Development of a Computational Tool for Simplifying Engineering Tradeoff Analysis for the Design of Cost-Optimized, Time-Variant, Electrodialysis Reversal Desalination Systems

by

Jeffrey Costello

Submitted to the Department of Mechanical Engineering
in partial fulfillment of the requirements for the degree of

Master of Science in Mechanical Engineering

at the

MASSACHUSETTS INSTITUTE OF TECHNOLOGY

September 2024

Authored by: Jeffrey Costello
Department of Mechanical Engineering
September 3, 2024

Certified by: Amos G. Winter V.
Associate Professor, Thesis Supervisor

Accepted by: Nicolas Hadjiconstantinou
Chairman, Department Committee on Graduate Theses

Development of a Computational Tool for Simplifying Engineering Tradeoff Analysis for the Design of Cost-Optimized, Time-Variant, Electrodialysis Reversal Desalination Systems

by

Jeffrey Costello

Submitted to the Department of Mechanical Engineering
on September 3, 2024, in partial fulfillment of the
requirements for the degree of
Master of Science in Mechanical Engineering

Abstract

This study presents an analytical tool for characterizing a wide swath of the design-space for time-variant electrodialysis reversal brackish water desalination (TEDR) while avoiding the computation time oft required by mechanistic models of electrodialysis reversal (EDR) and time-variant processes. In place of explicit computation, this paper proposes a simplifying assumptions to simulate desalination power and production rate of a TEDR process without explicit computation, enabling rapid year-long simulation and system optimization. The output of the model is compared to experimental data from a pilot TEDR system and found to have good agreement between desalination power and production rate. Disagreement between the modeled and experimental pressure losses suggesting additional losses in the experiment which may be accounted for in future work. Two case studies, one case for potable water in the American Southwest and another case for irrigation water in the Middle-East and North Africa (MENA) region, compare the results from 54 optimized systems. The results illustrate the complexity of system design and selection, elucidating trade-offs between different models of electrodialysis (EDR) stacks, operating modes, and system configurations. The output of this model will enable system designers to confidently design and implement cost-effective TEDR systems to combat rising global freshwater scarcity.

Thesis Supervisor: Amos G. Winter V.
Title: Associate Professor

Acknowledgments

This work has been funded by the **United States Bureau of Reclamation** through the Desalination and Water Purification Research Program. We thank them for their funding, support, and encouragement.

There is no combination, number, or selection of words which could adequately describe the indelible mark left on me by the GEAR Lab. This is very brief summary of the many people to whom I owe thanks.

First, Amos, I lack any of the necessary words to express my gratitude for your mentorship, camaraderie, enthusiasm, and kindness. The years I've spent with you, and the wonderful people of the GEAR Center, are the keystone to my character, both personally and professionally. Thank you, from the bottom of my heart, for your invitation to join this unforgettable, magical place. Twice.

Susan, your guiding hand has carefully pointed me toward intriguing problems which can only be solved with countless hours of deep, engaging thought. Your scrupulous attention to detail perfectly complements your kind, patient heart. I am graduating as a better scientist, owing no small part to each moment we worked together.

To the members of the Desal Team, past and present, thank you for your unwavering support. I have been pushed to my limits, through pilots and parametric models, and have emerged as a better engineer and better person. I owe an especial thanks to Melissa for her unconditional care and friendship through the countless trials we've faced through class and research.

To the members of the GEAR Lab, you are my best friends. My most cherished memories belong with Building 31 and with the incredibly talented, kind people who have graced its halls. I will sorely miss the unique enthusiasm I felt when arriving to the office each day, eager to work with the most incredible people in the world. Thank you for all the fun we've had, in the office, after hours, and around the world.

To all of my close friends: Thank you for making the bad times good and the

good times great.

To my brother, sister, partner, and all the pets we love so dearly: Thank you for your unmatched support and love.

To my mom and dad: You have pushed me and my siblings to the highest level of personal and professional achieve. There is not a world where I could have accomplished this degree without your support. Thank you for the incredible, lifelong scarifies you have both made for your children to ensure we are happy, healthy, and loved.

Contents

List of Figures

List of Tables

Roman Symbols	**Unit**	**Variable**
$C_{c,s}$	[mol/m^3]	concentrate concentration at the s$^{\text{th}}$ pass
$C_{d,s}$	[mol/m^3]	diluate concentration at the s$^{\text{th}}$ pass
C_{feed}	[mol/m^3]	feedwater concentration
c_p	[-]	pressure drop coefficient
$C_{d,prod}$	[mol/m^3]	product water concentration
crf	[-]	capital recoverty factor
F	[C/mol]	Faraday constant
f	[-]	friction factor
G_{brine}^{opex}	[USD/yr]	operating cost associated with brine disposal
G_{el}	[USD]	capital cost associated with electrodes
G_{mem}	[USD]	capital cost associated with membranes
G_{pc}	[USD]	capital cost associated with a pump controller
G_{PS}	[USD]	capital cost associated with a power supply
G_{pump}	[USD]	capital cost associated with a pump
G_{PV}	[USD]	capital cost associated with a PV panel
G_{sp}	[USD]	capital cost associated with flow spacers
G_{stack}	[USD]	capital cost associated with a stack
G_{sys}^{capex}	[USD]	CAPEX of the system
G_{sys}^{opex}	[USD]	OPEX of the system
G_{tk}	[USD]	capital cost associated with a tank
G_{WTP}^{capex}	[USD]	CAPEX of the WTP
G_{WTP}^{opex}	[USD]	OPEX of the WTP
$GHI(t)$	[W/m^2]	historical irradiance at time-step t
GHI_{design}	[W/m^2]	design irradiance level
GHI^{max}	[W/m^2]	maximum historical irradiance level
h	[m]	flow channel height
i	[A/m^2]	current density
I	[A]	electrical current
i_j	[A/m^2]	current density of the j$^{\text{th}}$ stack
I_j	[W]	electrical current of the j$^{\text{th}}$ stack
$i_{j,lim}^{+}$	[A/m^2]	limiting current density of the j$^{\text{th}}$ stack
i_{lim}	[A/m^2]	limiting current density
j	[-]	stack
J	[-]	last serialized stack in the system
k	[m/s]	boundary layer mass transfer coefficient
k_d	[-]	interest rate
L	[m]	flow path length
$LCOW_{WTP}$	[USD/m^3]	levelized cost of water of the WTP
m	[yr]	system lifetime
m_{pump}^{lower}	[-]	slope of pump penalty in the lower regime
b_{pump}^{lower}	[-]	intercept of pump penalty in the lower regime
m_{pump}^{upper}	[-]	slope of pump penalty in the upper regime
b_{pump}^{upper}	[-]	intercept of pump penalty in the upper regime
N	[-]	number of cell pairs
N_{abbPV}	[-]	number of PV panels
N_{sys}	[-]	systems in the WTP
$P_{c,hyd}$	[W]	concentrate hydraulic power
$P_{d,hyd}$	[W]	diluate hydraulic power
P_{hyd}	[W]	hydraulic power
$P_{j,desal}$	[W]	desalination power of the j$^{\text{th}}$ stack

Table 1: Roman Symbols

Roman Symbols	Unit	Variable
P_{PV}^{rated}	[W]	PV panel rated power
P_{PV}^{out}	[W]	PV array power output at time-step t
P_{sys}	[W]	system power consumption
P_{sys}^{max}	[W]	maximum system power consumption
P_{sys}^{min}	[W]	minimum system power consumption
Q	[m^3/s]	volumetric flow rate
Q_c	[m^3/s]	concentrate volumetric flow rate
Q_d	[m^3/s]	diluate volumetric flow rate
$Q_{d,sys}^{BEP}$	[-]	diluate flow rate at BEP
$Q_{d,sys}^{max}$	[m^3/s]	maximum system diluate flow rate
$Q_{d,arch}^{max}$	[m^3/s]	maximum architecture diluate flow rate
$Q_{d,sys}^{min}$	[m^3/s]	minimum system diluate flow rate
$Q_{d,arch}^{min}$	[m^3/s]	minimum architecture diluate flow rate
$\overline{Q}_p$	[m^3/s]	time-average water production rate
R^{AEM}	[Ωm^2]	AEM area resistance
R^{BL}	[Ωm^2]	area resistance of boundary layer
R^{CEM})	[Ωm^2]	CEM area resistance
r_0	[-]	current safety factor
$R_{c,s}^b$	[Ωm^2]	area restistance of bulk concentrate solution
$R_{d,s}^b$	[Ωm^2]	area restistance of bulk diluate solution
s	[-]	pass
S	[-]	total required number of passes
t^+	[-]	transport number of cations in solution
t^{mem}	[-]	counterion transport number of ions in IEMs
u_{ch}^{min}	[m/s]	minimum channel velocity
u_v	[m/s]	void channel velocity
V	[V]	voltage
V^{el}	[V]	electrode potential
V_j	[W]	voltage of the j^{th} stack
V_j^{AEM}	[V]	AEM potential
V_j^{CEM}	[V]	CEM potential
$\forall_{\nu,sys,}^{p}$	[m^3]	reliable daily system water production
$\forall_{\nu,WTP,target}^{p}$	[m^3]	water treatment plant reliable daily production target
$\forall_{sys,i}^{p}$	[m^3]	system water production on the i^{th} day of the year
W	[m]	flow path width
x_{bep}	[-]	design variable, pump best efficieny point
x_{ghi}	[-]	design variable, target irradiance level
x_{owl}	[-]	design variable, lower operating window
x_{owu}	[-]	design variable, upper operating window
z	[-]	ion charge number

Table 2: Roman Symbols, cont.

Greek Symbols	Unit	Variable
Δp_{total}	[Pa]	total pressure drop
Δp_j	[Pa]	pressure drop of the j^{th} stack
Δp_{loss}	[Pa]	other pressure losses
Δt	[s]	time-step duration of historical irradiance dataset
ϵ	[-]	flow spacer void fraction
η_{PS}	[-]	power supply efficiency
η_{pump}	[-]	pump efficiency
η_{pump}^{max}	[-]	maximum pump efficiency
η_{pump}^{Qmax}	[-]	pump efficiency at maximum system flow rate
η_{pump}^{Qmin}	[-]	pump efficiency at minimum system flow rate
ν	[-]	reliabililty
ϕ_a	[-]	flow spacer open-area porosity
ψ	[-]	architecture specific salt cut
ψ_0	[-]	stack independent salt cut
ψ_j	[-]	salt cut of the j^{th} stack
ξ	[-]	recovery ratio

Table 3: Greek Symbols.

Symbol	Meaning
AEM	anion exchange membrane
ASR	aquifer storage and recovery
BEP	pump best efficiency point
BGNDRF	Brackish Groundwater National Desalination Research Facility
CAPEX	capital cost
CEM	cation exchange membrane
DWI	deep well injection
EDR	electrodialysis reversal
GHI	global horizontal irradiance
IEM	ion exchange membrane
LCOW	levelized cost of water
MENA	Middle East and North Africa
NREL	National Renewable Energy Laboratory
NSRDB	National Solar Radiation Database
OPEX	operating cost
PV	photovoltaic
RO	reverse osmosis
SAWS	San Antonio Water System
SEC	specific energy consumption
TEDR	time-variant Electrodialysis reversal
TWDB	Texas Water Development Board
TX	Texas
WPC	water production characteristic
WTP	water treatment plant

Table 4: Abbreviations.

Chapter 1

Introduction

Brackish water desalination is increasingly being studied for its potential to alleviate worsening global freshwater scarcity caused by climate change, urbanization, and rapid population growth [2]. Electrodialysis reversal (EDR) desalination is a particular area of interest for EDR's high water recovery and low specific energy consumption (SEC) at brackish water salinities when compared to the more common reverse osmosis (RO) desalination [3, 4, 5]. Previous studies have found EDR desalination to have lower levelized cost of water (LCOW), measured in USD/m^3, for multiple applications including the production of potable water [6] and water for irrigation [7].

Within the context of climate change, there is increased interest to deliver desalinated water without reliance on fossil fuel-based energy sources, which lead to increased greenhouse gas emissions. This has contributed to increasing interest in photovoltaic- (PV) powered desalination [8]. PV-powered desalination is also being studied for its ability to serve resource-constrained communities with limited or unreliable access to grid power [9, 10]. Adapting existing desalination technologies to PV power requires costly energy storage to provide a consistent power level despite daily fluctuations and seasonal variations in irradiance [6].

Time-variant EDR desalination (TEDR) addresses this challenge by combining the water and energy efficient operation of EDR with its ability to closely match the power consumption of the system with the available power from a PV array, reducing or eliminating the need for an energy buffer, typically batteries [11, 12, 13]. Previous

studies have found the cost of water for a TEDR to be lower than a conventional PV-EDR systems with energy buffers and on-grid RO [11, 7]. In spite of TEDR's poise as a cost-effective, water-and-energy-efficient technology, one barrier to its adoption has been the identification and selection of cost-optimal TEDR systems.

Time-variant operation relies on changing the system's operating parameters to match the power consumption of the system with the availability of power from the PV array. Simulation models are used to predict the performance of TEDR systems, optimize their design characteristics, and thereby minimize the LCOW. Simulations iterate over small time steps to account for changes in the amount of power available and changes in the internal state of the system throughout the day. During each simulated time step, the mass balance of ions and water in the EDR stack must be evaluated using information from the previous time step. This is an explicit calculation and is solved sequentially in a for-loop within the computer code. One year of simulated performance requires 10s-of-millions of sequential computations often taking hours of computation time even on state-of-the-art computer hardware. The long computation time severely limits a system designer's ability to simulate various systems, evaluate the cost of alternative designs, and optimize to select the cost-optimal design.

To more efficiently and rapidly evaluate the broad TEDR design space, a model is required that is capable of predicting time-variant performance without explicit computation. The model does not need to be as accurate as previously reported models but should retain enough accuracy to identify the optimal system among many variations. Once the cost-optimial system is selected, a higher fidelity model could later be used to accurately predict system performance and cost.

This study first proposes number of model simplifications which will reduce computation time from hours of explicit computations to only 10s-of-milliseconds of parallel computations on the same computer hardware. The simplified model is then validated against experimental data from a small scale pilot EDR system. A second objective of the study is to establish a design methodology which quickly identifies viable TEDR architectures and use optimization to identify cost-optimal system char-

acteristics. The final objective is to use demonstrate the utility of the model in a series of case studies of interest. These case studies cover different applications of TEDR, feed and product water salinities, different daily and seasonal irradiance profiles, and two different size scales.

The resulting simplified TEDR model will enable system designers to make informed design decisions more quickly compared to previously reported models while retaining sufficient accuracy. The fast computation will allow for more systems to be simulated over year-long irradiance datasets enabling a more comprehensive search of the TEDR design space. This model can facilitate the use TEDR to create cost-effective solutions for brackish water desalination, facilitating the dissemination of this technology across multiple applications and markets, and help to combat global freshwater scarcity.

Chapter 2

Model description

This section presents a simplified model of TEDR performance as well as an optimization strategy that will enable a system designer to rapidly asses key trade-offs between multiple diverse system configurations and architectures. Multiple mechanistic models for the EDR process have been proposed and validated by previous studies, as reviewed by Campione et al. [3]. However, these models do not take into account time-variant operation and have not been designed to increase computational efficiency. The simplified model proposed here takes as its foundation a recent model of EDR performance proposed by Wright et al. [14] and a model of time-variant EDR performance proposed by He et al. [12]. Both the Wright et al. and He et al. models have been validated with experimental data collected from bench-top and pilot-scale EDR systems [14, 13, 15] and have been used to design cost-optimized EDR or TEDR systems [16, 17, 13]. However, due to the computation time required of these models they can not readily be used to design cost-optimal TEDR systems across the wide range of different configurations and architectures that might be of interest to a system designer be used to simulate a year of TEDR performance using historical irradiance.

2.0.1 Theory framework and definitions

EDR relies on an electrical field to move charged ions from a desalinated "diluate" solution to a concentrated "concentrate" solution by drawing ions across a series of alternating cation exchange membranes (CEM), which pass only cations, and anion exchange membranes (AEM), which pass only anions. The membranes are separated by mesh flow spacers that define the active flow path of water within the EDR unit, maintain the height of the flow channel, and promote water mixing. Each alternating series of AEM and CEM forms a "cell pair" and the stack of cell pairs between the electrodes form the EDR "stack."

Each EDR system is comprised of a number of individual EDR stacks in series. The system architecture is defined by the number of stacks in series, the stack model, the number of cell pairs in each stack, and the water recovery ratio. The recovery ratio is defined as the volume of product water per unit volume of feed water. The stack model prescribes factors such as the width and length of the membranes, flow channel height, electrode material, membrane material properties and other stack-specific properties.

In addition to architecture, each EDR system has a unique system configuration that is defined by four design variables, described fully in Section 2.0.5. A TEDR WTP is comprised of a specified number of TEDR "systems," each with a specified architecture and system configuration. The system configuration variables are optimized to design a TEDR water treatment plant (WTP) with the lowest LCOW that meets a set of performance targets. These performance targets include the concentration of the feed water, C_{feed} [mol/m^3], the desired concentration of the product water in the diluate, $C_{d,prod}$ [mol/m^3], fluid properties for the target solution (viscosity, density, etc.), a predefined system reliability, ν, and a targeted reliable daily production volume of product water for the WTP, $\forall^p_{\nu,WTP,target}$ [m^3]. The variable ν defines the number of days in a year that the system delivers a minimum volume of $\forall^p_{\nu,WTP,target}$.

An EDR system can be operated in either batch or continuous mode. A system operating in batch mode recirculates water, held in recirculation tanks, through the

stack(s) multiple times until the desired concentration is reached. A system operating in continuous mode achieves the desired product water concentration within a single pass through the series of EDR stacks in the system.

Each stack in an EDR system is numbered sequentially following the direction of flow of diluate using the variable j, where $j = 1$ is the first stack in series and $j = J$ is the last stack in series. This sequencing is illustrated in Figure 2-1 for both a batch and continuous system. The length of an individual stack is denoted as a single "pass." Each time the diluate completes a single pass, it becomes progressively less saline. The progressive number of passes, first through each individual stack j and then back through the series of stacks from the beginning, is denoted by s, with $s = 0$ denoting the inlet of the first stack. Within this framework, the outlet of stack $j = 1$ is denoted $s = 1$, as indicated in Figure 2-1. The bulk concentration for the diluate and concentrate channel associated with each pass is $C_{d,s}$ and $C_{c,s}$ [mol/m^3], respectively, and is evaluated at the outlet of the associated stack for the designated pass. S is defined as the total number of passes required to desalinate the diluate from the bulk feed water concentration at the start of the first pass, $C_{d,0} = C_{feed}$, to the desired bulk product water concentration at the end of the last pass, $C_{d,S} = C_{d,prod}$.

Within these definitions, a system operates in batch mode when the required number passes to achieve the desired product concentration is greater than the number of serialized stacks, or $S/J > 1$. A system operates in continuous mode when the number of passes is equal to the number of serialized stacks, $S/J = 1$. In some cases, a fractional number of passes is required to achieved the desired concentration.

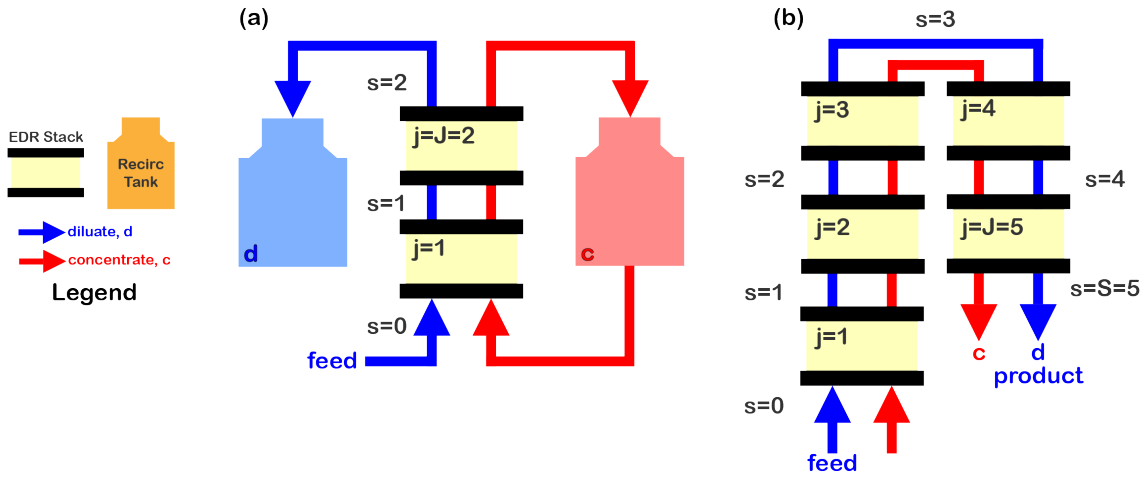

Figure 2-1: Schematic demonstrating two modes of operation, (a) batch and (b) continuous for a TEDR. Each EDR stack is numbered sequential from j to J following the direction of diluate flow. Passes s through S are ordered sequentially at the inlet and outlet of each stack. S is the total number of passes required to fully desalinate from the feed water concentration to the product water concentration. A system operates in batch mode when the total number of passes is greater than the number of serialized stacks, or $S/J > 1$, and requires recirculation tanks. A system operates in continuous mode when the number of passes equals the number of serialized stacks, or $S/J = 1$.

2.0.2 Simulating time-variant operation for a TEDR system

2.0.2.1 Time-variant framework

A TEDR simultaneously maximizes both the desalination rate and utilization of the PV power system during EDR operation with a variable power source [13]. It maximizes the desalination rate by maintaining a current density, i (defined as the current per unit membrane area), within the system that is as close as possible to the system's operating limit. This limit is defined by a limiting current density, i_{lim}, which is the current density at which water dissociation begins to occur. The TEDR system maximizes utilization of the PV power system by modulating pumping power and desalination power to match the available power from the PV array or another variable power source in real time. He et al. [13] demonstrated that two degrees of operational freedom - the system operating voltage, V [V], and volumetric flow rate, Q [m^3/s] - can be adjusted in real time to achieve both of these aims. A subsequent novel control scheme has been proposed and applied to a TEDR pilot system that controls the current applied, I, rather than voltage to achieve the same effect [15]. This study focuses on current-controlled TEDR because of computational simplicity and ease of implementation on real hardware. In contrast to TEDR operation, a fixed EDR system operates at a single operating flow rate. He et al. [13] details the many cost and performance benefits of time-variant operation over conventional fixed operation.

Conventional models of TEDR require prediction of the diluate and concentrate concentrations as well as power consumption at each iterative time step to predict the value of I and Q demanded by time-variant theory. To enable faster simulations and trade-off analysis, the simplified model proposed here constructs a system water production characteristic (WPC) that facilitates the selection of I and Q at each time step based only on the power available to the system. The system WPC relates the system power consumption to an average rate of water production following time-variant theory for a given architecture, system configuration, and performance targets. The WPC can be created at the start of a simulation and used as a lookup table to

assign a value of Q for each time step based on the available power, which is equal to the system power consumption in a TEDR system.

The TEDR theory outlined by He et al. can be applied to a system operated with any variable or constant power source, including a PV power source that incorporates energy storage through batteries. However, as a preliminary application, this study considers only TEDR system that directly utilize the available power source power with no energy buffer. This eliminates energy storage, which is typically one of the most expensive components of the power system. This scheme has been called "batteryless" or "direct-drive" TEDR in prior work [11]. Future work may incorporate energy storage, which is discussed in Sections 4 and 5.

2.0.2.2 Creation of a WPC for a TEDR system

The WPC relates the system power consumption to the average water production rate for an associated architecture, system configuration, and performance targets (i.e., feed and product water concentration). The flow rate of a real TEDR desalination process varies based on the instantaneous solar irradiance, as outlined in Section 2.0.2.1, making the average water production rate of a specific process difficult to predict. To estimate the WPC relationship, a simplification is made. For each potential flow rate that the system might operate, the average production rate of an equivalent batch process is used that operates at a constant flow rate and conforms to the current requirements of TEDR theory. This approach has been applied and validated in prior work [11]. In addition, the validity of this assumption is tested in Section 3.

The following sections outline the prediction of system power consumption as a function of the average water production rate for an equivalent batch process operating at a constant flow rate operating under TEDR constraints. This generates the WPC relationship for a specified architecture and performance targets that can be used to predict the total volume of desalinated water produced by a TEDR system over a year.

2.0.2.2.1 System power consumption

The system power consumption, P_{sys} [W], is the sum of the the total power consumed by the system for desalination and the power consumed for pumping. The total power for a system with hydraulic power consumption, P_{hyd}, and desalination power consumption of each individual stack, $P_{j,desal}$ is

$$P_{sys} = \frac{P_{hyd}}{\eta_{pump}} + \frac{1}{\eta_{PS}} \left(\sum_{j=1}^{J} P_{j,desal} \right) \ , \tag{2.1}$$

where η_{pump} is the efficiency of the pumps used to recirculate water and η_{PS} is the efficiency of the power supply used to power the EDR desalination process. The following sections outline methods to estimate each of these values for a given stack architecture, system configuration, and performance targets.

2.0.2.2.2 Desalination power for an EDR stack

The power required for desalination for each serialized stack j is

$$P_{j,desal} = I_j V_j \ , \tag{2.2}$$

where V_j [V] is the voltage applied to each stack j and I_j [A] is the electrical current applied to each stack j. The current applied to each stack is related to the current density and the available membrane area:

$$I_j = W L \phi_a i_j \ , \tag{2.3}$$

where L [m] is length of the flow path set by the flow spacer, ϕ_a is the open-area porosity of the flow spacer, and i_j [A/m^2] is the current density applied to stack j. The open-area porosity is a property of the mesh used to construct the flow spacer and is typically provided by the stack manufacturer.

For current-controlled TEDR processes, the applied current density is determined by $i^+_{j,lim}$, which is the limiting current density of stack j for positively charged ions in

solution, as

$$i_j = r_0 i^+_{j,lim} \ , \tag{2.4}$$

where r_0 is user-defined safety factor corresponding to a proportion of limiting current density. This safety factor protects against accidentally exceeding the limiting current density in the stack. Typically, r_0 is set to 0.7 and should not exceed 1 [18, 11]. For sodium chloride solutions, the limiting current density is estimated following Wright et al. [14] as

$$i^+_{j,lim} = \frac{zFkC_{d,s}}{t^{mem} - t^+} \ , \tag{2.5}$$

where z is the ion charge number; F [C/mol] is the Faraday constant, set to 96,485; t^{mem} is the counterion transport number for ions in the AEM and CEM; t^+ is the transport number of cations in solution; and k [m/s] is the boundary layer mass transfer coefficient. For sodium chloride solutions, $z = 1$, and this analysis follows Wright et al. to set $t^{mem} = 1$, and $t^+ = 0.39$ for sodium ions. These assumptions were validated against experimental data of EDR performance in natural groundwater [14].

We similarly adopt the derivation of Wright et al. [14] for k. Within this formulation, $k \propto Q_d^{0.5}$, where Q_d is the flow rate in the diluate channel. This scaling relationship for k relies on several empirically derived coefficients and exponents that depend on spacer and stack characteristics. These values were derived for one of the stack models used in this analysis, the Veolia Mark IV (MkIV) (discussed in Section 4).

The voltage applied to each stack V_j, is defined by an equivalent circuit analysis outlined in Wright et al. [14] as

$$
\begin{aligned}
V_j = V^{el} & \\
& + N(V_j^{AEM} + V_j^{CEM}) \\
& + \left(\frac{NI_j}{WL\phi_a}\right)(R_{d,s}^b + R_{c,s}^b + R^{BL} + R^{AEM} + R^{CEM}) \ ,
\end{aligned} \tag{2.6}
$$

where V_{el} is the electrode potential (caused by the reduction of hydrogen ions at the cathode and oxidation of chloride ions at the anode for a sodium chloride); N is the number of cell pairs in the stack; V_j^{AEM} and V_j^{CEM} [V] are the AEM and CEM membrane potentials for stack j, respectively; $R_{d,s}^b$ and $R_{c,s}^b$ [Ωm^2] are the bulk area resistances of the diluate and concentrate for pass s, respectively; R^{BL} is the area resistance of the boundary layers at the membrane surfaces; and R^{AEM} and R^{CEM} are the area resistances of the AEM and CEM, respectively, which are typically provided by the stack or membrane manufacturer. For this analysis, R^{BL} is assumed to be negligible. Wright et al. breaks the length of a single stack into a discrete number of segments for analysis; for the purpose of this simplified analysis, the number of segments is assumed to be 1 [14].

Functional forms of V_j^{AEM}, V_j^{CEM}, $R_{d,s}^b$, and $R_{c,s}^b$ are derived in Wright et al. for a single EDR stack based on stack-specific factors and the bulk concentration of diluate and concentrate channels at the start and end of each pass, $C_{d,s}$ and $C_{d,s+1}$ for the diluate, and $C_{c,s}$ and $C_{c,s+1}$ for the concentrate [14]. To estimate these values, this model proposes a simplification based on the "first pass" of desalination for each stack. This first pass occurs for all $s = j$. The simplification proposes that the desalination power of the first pass through each stack provides a reasonable first approximation of the total magnitude of stack power for all passes. With this simplification, only the values of $C_{d,s}$, and $C_{c,s}$ for $s = 0$ and $s = j$ need to be estimated.

To calculate the bulk concentrations of the first pass, the model first defines a salt cut, ψ_j, for stack j that characterizes the change in inlet and outlet bulk diluate concentration for the first pass ($s = j$):

$$\psi_j = 1 - (C_{d,s})/(C_{d,s-1}) \ . \tag{2.7}$$

From Wright et al., the change in diluate concentration across a single segment in a single stack depends on the rate of charged ion movement across the membranes, characterized by I_j, and factors that reduce the efficiency of the stack at translating current into salt removal, or stack efficiency factors. These stack efficiency factors are caused by effects such as back diffusion across the membranes due to the difference in concentration and fluid transport along the stack. This simplified model assumes a stack efficiency of 100%, enabling the concentration change in the stack to be characterized by

$$C_{d,s-1} = \frac{I_j N}{Q_d F z} + C_{d,s} \ . \tag{2.8}$$

By substituting Equations 2.3, 2.4, 2.5, and 2.8 into Equation 2.7, the salt cut is expressed as

$$\psi_j = 1 - 1/\left(\frac{WLN\phi_a r_0 k}{0.61 * Q_d} + 1\right) \text{ for all } j \ , \tag{2.9}$$

where 0.61 is the value for t^{mem} - t^+, adopting values for sodium chloride described above. Within this formulation, the salt cut is no longer a function of concentration, depending only on Q_d and architecture-specific parameters. In addition, the salt cut is the same for all j stacks in series within a single system. Therefore, ψ_j is renamed to exclude dependence on j as ψ_0.

Within this formulation for the first pass ($s = j$), the concentration $C_{d,s}$ is related to initial feed concentration, $C_{d,0} = C_{feed}$, through

$$C_{d,s} = C_{feed}(1 - \psi_0)^j \text{ for all } s = j \ . \tag{2.10}$$

The concentration of the concentrate channel, $C_{c,s}$, for pass s is assumed to the same as the feed water concentration during the first pass, or

$$C_{c,s} = C_{feed} \text{ for all } s = j \ . \tag{2.11}$$

This assumption presumes that the change in concentration for the concentrate channel in the first pass is small as a first-order estimation. Although this assumption is not likely to hold true, it will result in an underestimation of the concentration in the concentrate channel, which will increase steadily through the first pass. This underestimation will result in an underestimation of the area resistance in the concentrate channel, $R^b_{c,s}$, resulting in an overestimation of V_j through equation 2.6 and a conservative overestimation of the desalination power via equation 2.2.

A special consideration is made for systems for which the final attainable product diluate concentration in the last pass, $C_{feed}(1-\psi_0)^J = C_{d,S}$, is less than the desired product water concentration, $C_{d,prod}$. In this special case, a new salt cut is defined for each stack, ψ, that is adjusted to match and not exceed the required salt cut that would produce exactly the desired product concentration from the whole system. In this case, where $C_{d,S} \leq C_{d,prod}$, the system achieves its desired product concentration in one pass or less and the system is operating in continuous mode rather than batch mode. This is expressed as

$$\psi = \begin{cases} \psi_0 & \text{if } (1-\psi_0)^J < (C_{d,prod}/C_{feed}) \text{ Batch Operation} \\ 1-(C_{d,prod}/C_{feed})^{1/J} & \text{if } (1-\psi_0)^J \geq (C_{d,prod}/C_{feed}) \text{ Continuous Operation} \end{cases} . \tag{2.12}$$

With equation 2.12, ψ is a function that depends only on architecture-specific parameters, performance targets (e.g., C_{feed}, $C_{d,prod}$), and the flow rate in the diluate channel, Q_d. The concentrations at the inlet and outlet of each serialized stack during the first pass of operation are determined via equations 2.10 and 2.11, which are used to determine V_j^{AEM}, V_j^{CEM}, $R^b_{d,s}$, and $R^b_{c,s}$ of equation 2.6 for $s = j$. The voltage determined in equation 2.6 is combined with the current of equation 2.3 via equation 2.2 to estimate a value for $P_{j,desal}$. This calculation is analytical and does not require a time-series iteration.

2.0.2.2.3 Hydraulic power for an EDR system

The dominant hydraulic power requirement in an EDR stack is required to propel water through the diluate and concentrate channels at a flow rate of Q_d and Q_c in the diluate and concentrate channels, respectively. These flow rates are the same for each stack in series within a single system. To minimize pressure differentials across the membranes, EDR systems are typically operated such that the flow rate in each channel is equal, or $Q_d = Q_c$. The majority of the power requirement is needed to overcome pressure losses in the mesh spacers that fill the flow channels.

The total hydraulic power for the system, P_{hyd} [W], is the sum the hydraulic power required for the diluate, $P_{d,hyd}$ [W], and concentrate, $P_{c,hyd}$ [W], channels:

$$P_{hyd} = P_{d,hyd} + P_{c,hyd} \ . \tag{2.13}$$

The power required to sustain the flow of diluate and concentrate is determined by the flow rate and the total pressure drop across the system, Δp_{total} [Pa]:

$$P_{d,hyd} = Q_d(\Delta p_{total}) \ , \text{ and} \tag{2.14}$$

$$P_{c,hyd} = Q_c(\Delta p_{total}) \ . \tag{2.15}$$

The total pressure drop across the system considers the pressure drop across each stack in series, Δp_j [Pa], which is assumed to be equal for all stacks, as well as an additional term to account for pipe losses, tank head, and other sources of hydraulic loss in the system, Δp_{loss} [Pa], such that

$$\Delta p_{total} = J(\Delta p_j) + \Delta p_{loss} \ . \tag{2.16}$$

The proposed simplified model follows Wright et al. [14] in adopting a model of pressure losses across a single EDR stack proposed by Ponzio et al. [19]. This model has been experimentally validated for commercial stacks by Wright et al., where the measured pressure drop was found to deviate from predictions by approximately 37%

[14]. Despite the relatively large discrepancy, the Ponzio et al. model reproduced the expected behavior better than other considered models. Following this formulation, the pressure drop across each serialized stack is related to the Darcy-Weisbach prediction for flow between two parallel flat plates,

$$\Delta p_j = c_p \frac{\rho_{aq} f L u_v^2}{4h} \ , \tag{2.17}$$

where ρ_{aq} [kg/m^3] is the density of the aqueous solution; μ [Pa-s] is the viscosity of the aqueous solution; u_v [m/s] is the linear flow velocity for a flow channel devoid of a flow spacer [14]; f is the correlated friction factor from Ponzio et al. [19]; h is the height the flow channel; and c_p is a unique empirical coefficient adopted for this study. This empirical coefficient is set to $c_p = 1.59$ to reduce the 37% discrepancy between the experimental data and predicted pressure drop reported by Wright et al. [14]. The channel height, h, is assumed to be the equivalent to the thickness of the flow spacer, $h = h_{sp}$. The linear flow velocity, u_v, is proportional to Q_d as outlined in Wright et al., depending linearly on Q_d and other architecture-specific geometric factors. Using these equations, P_{hyd} for an EDR system can be predicted as a function of architecture-specific parameters, fluid-specific parameters, and Q_d.

2.0.2.2.4 Average water production rate

To complete the WPC relationship, the instantaneous diluate flow rate, Q_d, is converted to the average water production rate for an equivalent batch operating at constant flow rate. The time-average water production rate, $\overline{Q}_p$ [m^3/s], for the equivalent batch process is

$$\overline{Q}_p = Q_d \frac{J}{S} \ , \tag{2.18}$$

where S is a measure of the total number of passes required for the equivalent batch process to achieve the desired product water concentration, $C_{d,prod}$. This number is related to the single stack salt cut, ψ, as

$$S = \frac{\ln(C_{d,prod}) - \ln(C_{feed})}{\ln(1-\psi)} \ . \tag{2.19}$$

This estimated total number of passes is expected to be a lower bound due to factors that have not been considered in this analysis, such as inefficiencies of the stack, mixing within the recirculation tanks, water transport, and other factors. For a continuous system, S/J=1. The formulation of equation 2.18 allows for the equivalent batch process to be represented as a continuous process with a flow rate of $\overline{Q}_p$.

2.0.2.2.5 Architecture limitations and system configuration parameters

As noted in Section 2.0.2, each TEDR system is defined by an architecture (comprised of stack model, number of cell pairs per stack, number of stacks in series, and recovery ratio) and a system configuration. The system configuration is defined by four design variables or degrees of freedom that a system architecture has to deliver the desired performance targets, outlined in this section. These variables are optimized to design TEDR WIPs with the lowest LCOW in Section 2.0.5. These design variables are constrained by hardware limitations set by the system architecture.

There are a number of hardware limitations imposed by the system architecture. Each architecture has a minimum diluate flow rate determined by the stack model, $Q_{d,arch}^{min}$ [m^3/s]. The minimum diluate flow rate is defined by the minimum manufacturer recommended channel velocity, u_{ch}^{min} [m/s], which is related to the minimum diluate flow rate of the architecture by

$$Q_{d,arch}^{min} = u_{ch}^{min} \epsilon W h N \ , \tag{2.20}$$

where ϵ is the void fraction of the mesh used to construct the flow spacer. The minimum channel velocity used by this model is 7 cm/s, which is recommended by the stack manufacturer [14]. The void fraction is also provided by the stack manufacturer. This minimum flow velocity ensures the solution in the flow channel well-mixed by turbulent flow, promoting ion exchange and reducing the risk of fouling

[20]. In addition, each stack model has a maximum diluate flow rate, $Q_{d,arch}^{max}$ [m^3/s], imposed by pressure limitations on the spacers or voltage capacity of the particular stack set by the manufacturer. High pressure can cause internal leakage within the stack, external stack leakage, or stack instability which can cause the membranes or flow spacers to shift relative to the electrodes. The hardware limits of stacks used in this study are reported in Section 4.

On top of these hardware constraints, the first two degrees of freedom that define the system configuration further constrain the system flow rate to operate within a narrower range. Choosing to operate over a narrower flow rate range allows the system to consider known trade-offs between the SEC of the desalination process and the power consumption level of the TEDR system. The first degree of freedom is the lower operating window, x_{owl}. This is defined as a fraction (reported as a percentage) of the operating window determined by the hardware constraints, setting a more constrained minimum volumetric flow rate of the *system*, $Q_{d,sys}^{min}$ [m^3/s], as opposed to the hardware constraint of the *architecture*, $Q_{d,arch}^{min}$. Similarly, the upper operating window, x_{owu}, is a fraction (reported as a percentage) of the architecture-constrained operating window that sets the maximum volumetric flow rate of the system, $Q_{d,sys}^{max}$, which may be more constrained than the maximum flow rate limit of the architecture, $Q_{d,arch}^{max}$. These system configuration variables are related to the diluate flow rates of the architecture and system by

$$Q_{d,sys}^{min} = x_{owl}(Q_{d,arch}^{max} - Q_{d,arch}^{min}) + Q_{d,arch}^{min} \text{ provided } x_{owl} \leq x_{owu} \text{ , and} \tag{2.21}$$

$$Q_{d,sys}^{max} = x_{owu}(Q_{d,arch}^{max} - Q_{d,arch}^{min}) + Q_{d,arch}^{min} \text{ provided } x_{owu} \geq x_{owl} \text{ .} \tag{2.22}$$

The time-variant system operates within the constraints $Q_{d,sys}^{min} \leq Q_d \leq Q_{d,sys}^{max}$. If the lower and upper operating windows are the same, or $x_{owl} = x_{owu}$, the system operates at a fixed flow rate rather than as a time-variant system. The maximum

system power consumption, P_{sys}^{max} [W], and minimum system power consumption, P_{sys}^{min} [W], are determined from $Q_{d,sys}^{max}$ and $Q_{d,sys}^{min}$, respectively, according to equations 2.1 - 2.30.

The third degree of freedom in the system configuration is the pump best efficiency point (BEP), defined by the variable x_{bep}. This value reflects that a centrifugal pump, commonly used in desalination systems, does not operate at a uniform efficiency over its entire range of operation. The variation in efficiency is particularly pronounced when the pump's speed is controlled by a variable frequency drive or motor controller. A pump which is least efficient at the maximum system flow rate, $Q_{d,sys}^{max}$, results in the highest power consumption. A higher power consumption increases the size and capital cost of the required PV power system as well as the size and capital cost of the pump. The trade-off between pump operating point and efficiency depends sensitively on the specific make and model of the selected pump. To capture this trade-off without pre-defining or pre-selecting a pump with a specific make and model, this simplified model incorporates a double-linear penalty on pump efficiency relative to the best efficiency point. This penalty is expected to capture the first-order effects of a realistic pump efficiency curve.

The x_{bep} variable is defined as a fraction (reported as a percentage) of the system flow rate operating window. This value determines the flow rate at which the pump will be most efficient, $Q_{d,sys}^{BEP}$, which is defined as

$$Q_{d,sys}^{BEP} = x_{bep}(Q_{d,sys}^{max} - Q_{d,sys}^{min}) + Q_{d,sys}^{min} \ . \tag{2.23}$$

This value is then used to define the efficiency penalty as the flow rate deviates from $Q_{d,sys}^{BEP}$. The efficiencies of the pump at the minimum and maximum system flow rate, η_{pump}^{Qmin} and η_{pump}^{Qmax} respectively, are defined by

$$\eta_{pump}^{Qmin} = \eta_{pump}^{max}\left(\frac{x_{bep} * Q_{d,arch}^{min}}{Q_{d,arch}^{max}} - x_{bep} + 1\right) \ , \text{ and} \tag{2.24}$$

$$\eta_{pump}^{Qmax} = \eta_{pump}^{max}\left(-\frac{x_{bep} * Q_{d,arch}^{min}}{Q_{d,arch}^{max}} + x_{bep} + \frac{Q_{d,arch}^{min}}{Q_{d,arch}^{max}}\right) \ , \tag{2.25}$$

where η_{pump}^{max} is the maximum pump efficiency. The slopes of the double-linear penalty are calculated separately for flow rates lower than $Q_{d,sys}^{BEP}$, the lower flow regime, and flow rates greater than $Q_{d,sys}^{BEP}$, the upper flow regime. The slopes m_{pump}^{lower} and m_{pump}^{upper} of the lower and upper regimes, respectively, are defined by

$$m_{pump}^{lower} = \frac{\eta_{pump}^{max} - \eta_{pump}^{Qmin}}{Q_{d,sys}^{BEP} - Q_{d,sys}^{min}} \ , \text{ and} \tag{2.26}$$

$$m_{pump}^{upper} = \frac{\eta_{pump}^{Qmax} - \eta_{pump}^{max}}{Q_{d,sys}^{max} - Q_{d,sys}^{BEP}} \ . \tag{2.27}$$

The intercepts of the double-linear penalty for the lower and upper flow regimes, b_{pump}^{lower} and b_{pump}^{upper}, respectively, are defined by

$$b_{pump}^{lower} = \eta_{pump}^{max} - m_{pump}^{lower}\left(Q_{d,sys}^{BEP}\right) \ , \text{ and} \tag{2.28}$$

$$b_{pump}^{upper} = \eta_{pump}^{max} - m_{pump}^{upper}\left(Q_{d,sys}^{BEP}\right) \ . \tag{2.29}$$

This results in the following general expression for the pump efficiency at any flow rate,

$$\eta_{pump} = \begin{cases} m_{pump}^{lower}\left(Q_d\right) + b_{pump}^{lower} & \text{for } Q_d \text{ s.t. } Q_{d,sys}^{min} \leq Q_d < Q_{d,sys}^{BEP} \\ m_{pump}^{upper}\left(Q_d\right) + b_{pump}^{upper} & \text{for } Q_d \text{ s.t. } Q_{d,sys}^{BEP} \leq Q_d \leq Q_{d,sys}^{max} \end{cases} . \tag{2.30}$$

This pump efficiency is used in equation 2.1.

This formulation of the pump efficiency leads to two notable effects. First, the magnitude of the pump efficiency penalty is affected by the magnitude of the maximum system flow rate relative to the minimum system flow rate, or $Q_{d,sys}^{max}/Q_{d,sys}^{min}$. This reflects the realistic efficiency performance penalty of operating over a wider range of flow rates with a single pump. Second, the magnitude of the penalty at the minimum and maximum system flow rate depends on the value of x_{bep}. As an

example, a x_{bep} of 30% applies 30% of the total penalty to the minimum flow rate and 70% of the total penalty to the maximum flow rate. This reflects that the pump efficiency typically reduces in magnitude as the flow rate deviates farther from the BEP.

The final degree of freedom in the system configuration defines a target irradiance, x_{ghi}. This value sets a design irradiance level, GHI_{design} [W/m^2], as the solar irradiance at which the power output from the PV array matches the maximum power consumption of the system, based on the rated power of the solar panels. Power generated at an irradiance in excess of the design irradiance level cannot be utilized by the system. The variable x_{ghi} is defined as a fraction of the maximum solar irradiance (reported as a percentage) in the year of historical weather data used to benchmark TEDR performance, defined as GHI^{max}. Thus

$$GHI_{design} = x_{ghi} GHI^{max} \ . \tag{2.31}$$

From this value, the required number of PV panels, N_{PV}, necessary to generate the maximum system power requirement, P_{sys}^{max}, is defined as

$$N_{PV} = P_{sys}^{max} / \left(\frac{GHI_{design} P_{PV}^{rated}}{1000} \right) \ , \tag{2.32}$$

where P_{PV}^{rated} [W] is the manufacturer rated power of the solar panel at 25°C and 1000 W/m^2 irradiance. The output of the PV array is assumed to scale linearly with the available irradiance [21].

The four degrees of freedom that make up the system configuration are summarized in Table 2.1, along with the bounds and resolution applied to the system optimization, described in Section 2.0.5.

Variable	Symbol	Bounds	Resolution
Lower Operating Window Threshold	x_{owl}	0-100%	0.1%
Upper Operating Window Threshold	x_{owu}	0-100%	0.1%
Pump Best Efficiency Point	x_{bep}	0-100%	0.1%
Target Irradiance Level	x_{ghi}	0-100%	0.1%

Table 2.1: The four degrees of freedom, or design variables, that determine the TEDR system configuration. The bounds of each variable are reported along with the resolution applied during system optimization.

2.0.3 Water treatment plant performance outcomes

The equations outlined in Section 2.0.2.2 define a WPC that relates the system power consumption to the average water production rate for a TEDR system with a specified architecture, system configuration, and performance targets (C_{feed}, $C_{d,prod}$, fluid properties, ν, $\dot{V}^{p}_{\nu,WTP,target}$). This WPC is then combined with a year of historical solar irradiance data to determine the total volume of desalinated water produced by a TEDR that meets the performance targets over the year.

To determine the annual volume of water delivered by the TEDR system, the WPC is combined with a dataset of yearly irradiance particular to a geographic location. The solar irradiance dataset is converted to the power output of a PV array, P^{PV}_{out}, that is divided into time steps with resolution Δt. The power output of the PV array is defined as

$$P^{PV}_{out} = \frac{N_{PV} P^{rated}_{PV} GHI(t)}{1000} \ , \tag{2.33}$$

where $GHI(t)$ is the historical irradiance for each time step of the solar irradiance dataset. For each time step, if P^{PV}_{out} is less than P^{min}_{sys}, the system remains off during that time step and generates no desalinated water. If P^{PV}_{out} is greater than P^{max}_{sys}, the system power consumption is assumed to be P^{max}_{sys}. For output power levels $P^{min}_{sys} \leq P^{PV}_{out} \leq P^{max}_{sys}$, then P^{PV}_{out} is set to be equal to P_{sys} of equation 2.1. The WPC relationship defined in Section 2.0.2.2 is then used to determine $\overline{Q}_p$ associated

with each power level P_{out}^{PV} and an incremental volume of water $\Delta t\overline{Q}_p$ is added to the volume of water produced by the TEDR system for each time step. The volume of water produced by the system each day, i, is $\forbar{V}_{sys,i}^{p}$ [m^3], which is the sum of the incremental volumes of water produced during each time step over each day of historical weather data.

After evaluating the set of data $\forbar{V}_{sys,i}^{p}$, the reliable daily water production of the system, $\forbar{V}_{\nu,sys}^{p}$ [m^3], is evaluated at the percentile $1-\nu$ within the dataset, where ν is the desired system reliability set by the performance targets.

The desired reliable daily production of the WTP, $\forbar{V}_{\nu,WTP,target}^{p}$, is set by the performance requirements outlined in Section 2.0.2. If $\forbar{V}_{\nu,sys}^{p} < \forbar{V}_{\nu,WTP,target}^{p}$, the required number of systems necessary to meet the WTP target, N_{sys}, is defined by

$$N_{sys} = \left\lceil \frac{\forbar{V}_{\nu,WTP,target}^{p}}{\forbar{V}_{\nu,sys}^{p}} \right\rceil , \tag{2.34}$$

where the brackets indicate that the result must be rounded up to the nearest integer value.

The final performance outcome is the mode of operation. At any time step, a TEDR system and WTP may operate in batch or continuous mode, based on the value of S/J, where S is defined in equation 2.19. As noted in Section 2.0.2, a value of $S/J > 1$ indicates batch mode and $S/J = 1$ indicates continuous mode. If the system WPC switches between operating modes, depending on its flow rate and, thereby, its power consumption, it is considered to be a mixed mode system.

2.0.4 Cost model

The cost model defines an LCOW based on component cost inputs particular to a given geographic location and the performance outcomes determined in Section 2.0.3. The LCOW calculation for the WTP, $LCOW_{WTP}$ [USD/m^3], follows Lienhard et al. [22], and is defined as

$$LCOW_{WTP} = \frac{crfG_{WTP}^{capex} + G_{WTP}^{opex}}{365\forbar{V}_{\nu,WTP,target}^{p}} , \tag{2.35}$$

where where crf is a capital recovery factor; G_{WTP}^{capex} [USD] is the total capital cost of the WTP; and G_{WTP}^{opex} [USD/year] is the total operating cost over one year of operation.

The crf is an amortization factor on the capital cost

$$crf = \frac{k_d(1+k_d)^m}{(1+k_d)^m - 1} \ , \tag{2.36}$$

where k_d is the annual interest rate; and m is the depreciation period, which is set to be the expected system lifetime.

The system capital cost, G_{sys}^{capex} [USD], is defined as

$$G_{sys}^{capex} = \begin{cases} JG_{stack} + \sum_{j=1}^{J} G_{j,PS} + 2(G_{pump} + G_{pc} + G_{tk}) + N_{PV}G_{PV} & \text{if Batch or Mixed} \\ JG_{stack} + \sum_{j=1}^{J} G_{j,PS} + 2(G_{pump} + G_{pc}) + N_{PV}G_{PV} & \text{if Continuous} \end{cases} , \tag{2.37}$$

provided the cost of the stack, G_{stack}, is

$$G_{stack} = 2N(G_{sp} + G_{mem}) + 2G_{el} \ . \tag{2.38}$$

$G_{j,PS}$ is the cost of the stack power supply for the j$^{\text{th}}$ stack; G_{pump} is the cost of the pump; G_{pc} is the cost of pump controller; G_{tk} is the cost of the tank; G_{PV} is the cost of a single solar panel; G_{sp} is the cost of a single spacer; G_{mem} is the capital cost of a single membrane; and G_{el} is the capital cost of a single electrode. Each system is comprised of two pumps, each with a pump controller; a power supply appropriately rated for the power requirements of the j$^{\text{th}}$ stack; and an PV array comprised of N_{PV} panels. The capital cost of two recirculation tanks is only included for system that which operate in batch or mixed mode. The cost of tanks are not included for systems that operate in continuous mode. For the calculation of stack cost, each cell pair, N, requires one AEM, one CEM, one flow spacer for the diluate flow channel, and one flow spacer for the concentrate flow channel, or $2N$ of each component. Each stack requires two electrodes. The capital cost of the WTP is the sum of the capital cost of N_{sys} systems, or $G_{WTP}^{capex} = N_{sys}G_{sys}^{capex}$.

Component capital costs scale in different ways: electrode, membrane, and spacer costs scale with stack area [m^2]; power supply costs scale with maximum power output [W]; pump costs and pump controller costs scale with rated maximum pump power [W]; and PVpanel costs scale with the number of required solar panels [W]. The specific functional form of the scaling and coefficients depend on the local cost of products available in the geographic location of interest. Component cost models used for this study are presented in Section 4. Storage tanks for batch recirculation are assumed to be a fixed cost applied to each batch or mixed mode system; each batch or mixed system requires 2 tanks of 1 m^3 each, which are sufficient to meet the needs of all system scales considered in this study (each tank costs $880).

The yearly operating cost for the WTP, G_{WTP}^{opex} [USD/yr], is defined as

$$G_{WTP}^{opex} = N_{sys} G_{sys}^{opex} \ , \tag{2.39}$$

where G_{sys}^{opex} is the yearly operating expense of each TEDR system. For this study, the only operating cost considered is the cost of brine disposal:

$$G_{sys}^{opex} = G_{brine} \ , \tag{2.40}$$

where G_{brine} [USD/yr] and is the cost of brine disposal per unit volume of brine generated. This cost scales with the volume of brine produced per day, $\dot{V}_{\nu,sys}^{b}$. The volume of brine generated can be calculated using mass balance and the recovery ratio, ξ, as

$$\dot{V}_{\nu,sys}^{b} = \dot{V}_{\nu,sys}^{p} \left(\frac{1}{\xi} - 1 \right) \ . \tag{2.41}$$

The case-specific cost of brine disposal is covered in Section 4.

2.0.5 Architecture identification and System Optimization

An optimization is performed to identify values of the four design variables described in Section 2.0.2.2.5 that meet the defined performance requirements with a minimum

$LCOW_{WTP}$. A genetic algorithm (GA) was applied in MATLAB.

Replicate results tended to converge on a value for the WTP LCOW. The algorithm was replicated 15 times with the conditions outlined in Section 4.1, resulting in system designs with a standard deviation of the WTP LCOW of \$0.0076 USD/m^3. This value was adopted as a measure of uncertainty due to the stochastic output expected for GA. The algorithm considered systems with a limited number of stacks in series, based on the architecture and system configuration. Starting with one stack, the number of stacks was incremented until the system could achieve continuous operation over the entire range of diluate flow rates defined by the upper and lower system flow rate limits, as defined in Section 2.0.2.2.5.

Chapter 3

Model validation

The simplified model of TEDR performance outlined in Section 2 makes a number of strategic simplifying assumptions to promote computational efficiency. To understand the impact that these assumptions could make on prediction accuracy, model predictions were compared to experimental measurements collected during operation of a pilot-scale, PV-powered, direct-drive, TEDR system deployed in the summer of 2022 in Alamogordo, New Mexico [15].

The pilot system was comprised of a single commercial Veolia model V20 EDR stack with 150 cell pairs operated in batch mode. The system was operated over 157 days fed with real brackish groundwater from Well 1 at the Brackish Groundwater National Desalination Research Facility (BGNDRF). The average feed water conductivity during the experiments was 1800 μS/cm. The target product water conductivity was 1000 μS/cm, with an average measured product water conductivity throughout the trial of 966 μS/cm. Full details of system specifications, experimental methodology, and performance targets are reported previously [15].

3.0.0.1 Comparison of desalination power

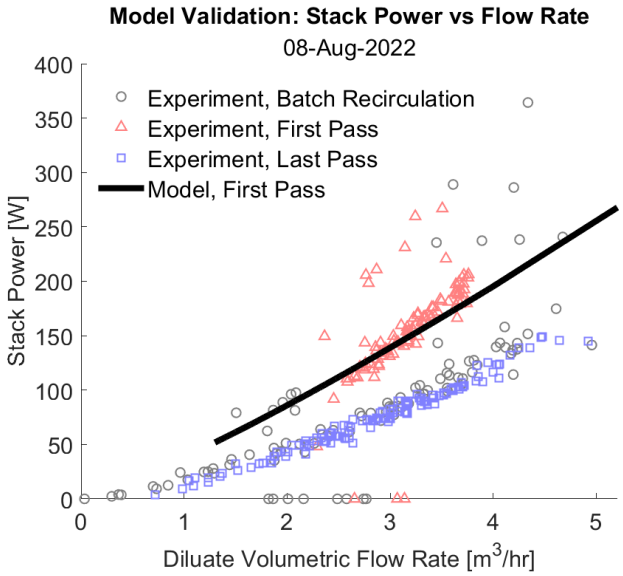

Figure 3-1: Modeled versus experimental desalination power for one day of operation of a pilot TEDR system. The first pass occurs during the filling state, distinguished as red triangles. During the first pass, the experiment was drawing water in from the feed source through the stack and into the recirculation tanks. The modeled desalination power has good agreement first pass power.

Day	First Pass Avg Diff	Last Pass Avg Diff	Batch Recirc. Avg Diff	All Data Avg Diff
August 8, 2022	-3.7%	83%	49%	47
August 18, 2022	-3.7%	82%	49%	41
August 23, 2022	-3.9%	77%	47%	36
August 25, 2022	-2.1%	73%	44%	34

Table 3.1: Average difference between modeled and experimental data for desalination power. The average difference is the fraction (reported as a percent) which the model over- or under-predicts the experimental desalination power.

The measured power consumption as a function of diluate volumetric flow rate for the pilot desalination unit on a representative day (August 8, 2022) is presented in

Figure 3-1. Power consumption is reported during the first pass, last pass, and during batch recirculation. The comparison demonstrates good agreement between the model-predicted desalination power for the first pass and the experimentally measured desalination power. The average difference between model predictions and experimental data for four of the operating days is presented in Table 3.1. The agreement during the first pass is quite high, with an average difference of 2.1 - 3.7%. When the modeled power is compared with the last pass and batch recirculation, the average difference ranges from 73% to 83% and 44 to 49% respectively. The modeled predicted consumption when considering all data ranging from 34 - 47%. As noted in Section 2.0.2.2.2, the simplifying assumptions made in the model were expected to overestimate the power consumption of the desalination process during batch recirculation, the last pass, or when considering all data. The output of the model has the intended behavior.

The impact of conservative estimate of stack power consumption for the entire desalination process suggest the model will overestimate the LCOW due to stack power, providing a conservative estimate. Additional days of comparison are provided in the Appendix, Section A, all with similar levels of agreement.

3.0.0.2 Comparison of hydraulic power

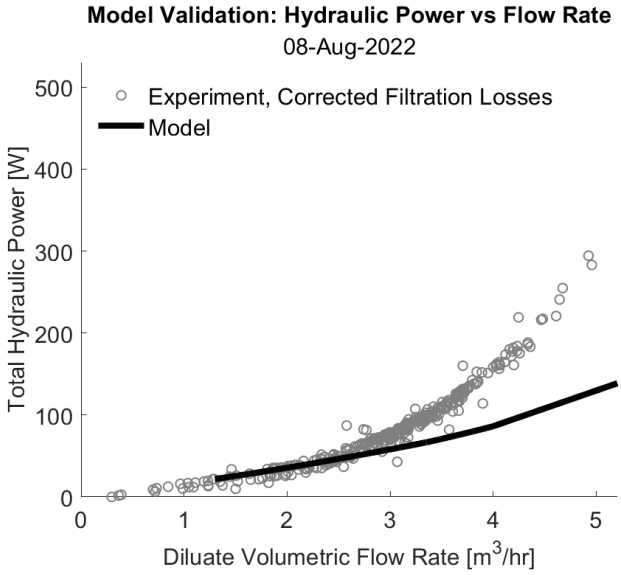

Figure 3-2: Modeled versus experimental hydraulic power versus diluate flow rate for one day of operation for a pilot TEDR system. The experimental data has one correction factor to account for higher-than-expected filtration losses. As volumetric flow rate increases, the modeled hydraulic power is less accurate suggest there are other losses in the system not accounted for in the model. Positive values indicate the over-prediction by the model.

Day	Avg. Diff.
August 8, 2022	-20%
August 18, 2022	-24%
August 23, 2022	-21%
August 25, 2022	-28%

Table 3.2: Average difference between modeled and experimental data for hydraulic power. The average difference is the fraction (reported as a percent) which the model over- or under-predicts the experimental hydraulic power. Positive values indicate the over-prediction by the model.

Figure 3-2 compares the diluate volumetric flow rate to the hydraulic power required to achieve that flow rate, as measured in the pilot EDR system. A correction was made to account for higher than expected pre-filtration pressure losses in pilot system. This was due to an undersized filter for the purpose. The correction was made by measuring the pressure drop across the pre-filter alone while the pilot system was operated without desalinating over a range of flow rates. This pressure drop was converted to a hydraulic power and subtracted from the measured data.

The model tends to underestimate total hydraulic power, particularly at higher flow rates. This is consistent with prior work, which found a similar discrepancy between modeled hydraulic power and measured hydraulic power in a pilot-scale EDR system [14]. The discrepancy suggests that other pressure losses exist in the system that are not accounted for in the model. Future research can consider adding a major pipe loss model to account for the piping connecting the pumps, stack, and tanks. A comparison between model predictions and data on four other representative days was consistent (Table A.3), resulting in a model underestimate of 20 - 28%.

Due to this discrepancy, the model is likely to underestimate LCOW compared to real desalination systems, particularly systems with a large maximum system flow rate. A real system will have to incorporate larger than modeled pumps and PV arrays to accommodate the higher hydraulic power. However, there is very good agreement between the model and experimental data at lower flow rates.

3.0.0.3 Water production rate validation

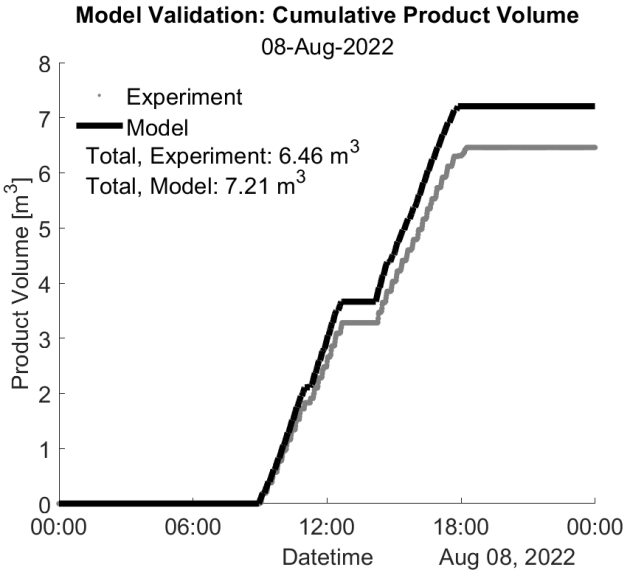

Figure 3-3: Modeled and experimental cumulative water production versus time for one day of operation of a pilot TEDR system.

Day	Experiment [m^3]	Model [m^3]	Difference
August 8, 2022	6.46	7.21	12%
August 18, 2022	5.99	5.97	-0.3%
August 23, 2022	4.46	4.99	12%
August 25, 2022	7.1	7.81	10%

Table 3.3: The difference in the modeled total product volume versus experimental total product volume.

Figure 3-3 demonstrates good agreement between the model-predicted total volume of water produced and measured volume of water produced in the pilot system. The trend of water production over time is also reproduced. Additional comparisons of the daily total volume of water produced are presented in Table 3.3, which also demonstrate good agreement. This level of agreement suggests that the model may be able to capture key performance trends despite the simplifications, enabling it to distinguish the performance of difference system architectures.

The tendency of the model to predict a slightly higher daily water production volume compared to experiment reflects the assumption in the model of a 100% stack efficiency, described in Section 2.0.2.2.2. This assumption will cause the model to underestimate the power requirement to desalinate, predicting that more water can be produced at the same power level relative to the experiment. The impact of an over-prediction in daily production will be an under-prediction of LCOW, as each system will be able to amortize its own cost by producing more water, requiring fewer systems to meet the WTP target production.

Chapter 4

Case studies

Two case studies of interest have been defined to demonstrate the capability of this model to select cost-optimal a TEDR system from a number of alternative designs. The diversity of needs in each case illustrate the need for a robust methodology for optimization and trade-off analysis. The first case focuses on the application of TEDR desalination to supply potable water for Elmendorf, Texas. The second case focused on desalination for irrigation in Qena, Eygpt. Results from sensitivity analysis for Elmendorf, Texas will also be presented.

Abbreviation	Manufacturer	Model	No. Cell Pairs
MkIVx600	Veolia	MkIV-2	600
MkIVx400	Veolia	MkIV-2	400
MkIVx200	Veolia	MkIV-2	200
V20x300	Veolia	V20	300
V20x150	Veolia	V20	150
V20x100	Veolia	V20	100

Table 4.1: The list of commercially available EDR stacks explored in this study, limited to those manufactured by Veolia Water Technologies [1]. Each stack is configured with a different number of cell pairs. The V20 is a smaller EDR stack with a flow path length that is 30% of the MkIV flow path.

Parameter	MkIV	V20	Unit
Flow Path Length, L	1.68	0.508	[m]
Flow Path Width, W	0.197	0.2032	[m]
Membrane Length, L_{mem}	1.016	0.75	[m]
Membrane Width, W_{mem}	0.4699	0.35	[m]
Electrode Potential, V_{el}	1.4	1.4	[V]
Mininum Channel Velocity, u_{ch}^{min}	0.07	0.07	[m/s]
Maximum Inlet Pressure, ΔP^{max}	344738	344738	[Pa]
CEM	Veolia, CR67E	Veolia, CR67T	[-]
AEM	Veolia, AR204E	Veolia, AR204T	[-]
CEM Area Resistance, R_{CEM}	0.00055	0.00025	[Ohm-m^2]
AEM Area Resistance, R_{CEM}	0.00032	0.00017	[Ohm-m^2]
Flow Spacer Void Fraction, ϵ	0.83	0.83	[-]
Flow Spacer Open Area Porosity, ϕ_a	0.7	0.7	[-]
Flow Spacer Thickness, h_{sp}	0.00071	0.00078	[m]

Table 4.2: List of stack-specific parameters used to calculate the performance of each stack.

For these two cases, two models of commercially available EDR stacks produced by Veolia Water Technologies were considered, the MkIV and V20 [1]. Stack specific parameters, such as dimensions of the flow path and thickness of the flow spacers are tabulated in Table 4.2. The MkIV is a larger stack that can be configured with up to 600 cell pairs. The V20 is a smaller, cheaper stack that can be configured with up to 300 cell pairs. For each stack, three commercially-available configurations of cells pairs were selected to evaluate the impact of cell pairs on the WTP LCOW. Stacks with fewer cell pairs have a lower capital cost but reach their maximum rated inlet pressure at lower flow rates, limiting their range of operation. Valid architectures were defined for each of the six models of stack presented in Table 4.1 abiding by the constraints for valid architecture set in Section 2.0.5. Each valid architecture

was then optimized, using the design variables in Table 2.1, resulting in alternative designs for a cost-optimized WTP.

In both cases, the targeted reliability was 95%. At higher reliabilities, the cost of water increases sharply as a fewer, low-irradiance days disproportionately effect number of systems required to meet the targeted daily production of the WTP.

Cost Model	Type	Value
Pump	CAPEX, USD	$G_{pump} = -5705.3 + 1084.1ln\left(\frac{P_{hyd}^{max}}{1000\eta_{pump}^{Qmax}}\right)$
Pump Controller	CAPEX, USD	$G_{pc} = 0.0961\left(\frac{P_{hyd}^{max}}{1000\eta_{pump}^{Qmax}}\right) + 345.42$
Stack Power Supply	CAPEX, USD	$G_{J,PS} = 0.5015\left(\frac{P_{j,desal}^{max}}{1000\eta_{PS}}\right) + 49.282$
Membrane	CAPEX, USD	$G_{mem} = 75L_{mem}W_{mem}$
Electrode	CAPEX, USD	$G_{el} = 1200LW$
Spacer	CAPEX, USD	$G_{sp} = 23L_{mem}W_{mem}$
Tank	CAPEX, USD	$G_{tk} = 880$
PV Panel	CAPEX, USD	$G_{PV} = 500$

Table 4.3: The capital cost model used to determined the component costs of the system and WTP.

The component capital cost models utilized for both cases is presented in Table 4.3. These component costs contribute to the LCOW as outlined in Section 2.0.4. The cost of brine disposal was determined by the most cost-effective brine disposal method available in each geographic region, reported in Sections 4.1 and 4.2 for each

case study. The cost of the membranes are calculated from the actual membrane length and width. The additional membrane area is required on the perimeter of the flow path to create a fluid-tight seal with the flow spacer. The flow spacer has the same dimensions as the membrane. The electrode area is calculated from the length and width of the flow path. The cost of the pump, pump controller, and stack power supply are calculated by the maximum power consumption of each respective component.

The capital costs used for the pump, pump controller, stack power supply, and tanks were aggregated from several online resources. For each cost function, a curve of best fit was applied with either a logarithmic fit or polynomial fit up to the 3rd degree. The best fit function, logarithmic or polynomial, was selected according to the highest R^2 value. The capital cost of the pumps were extracted from the online supplier, Grainger, using their catalog of three-phase, centrifugal pumps from the supplier Goulds. The pumps ranged in rated electrical power from 0.3 kw to 15 kW [23]. WEG variable frequency drives ranging from 0.2 to 83 kW supplied by Automation Direct were used to model the cost of the pump controller [24]. The cost of AC/DC power converters from Digikey ranging from 2 to 17 kW were used to estimate the cost of the stack power supply [25]. The cost of a 1 m^3 tank was estimated using US Plastic Corporation's selection of IBC tote tanks ranging from 0.1 to 1.3 m^3 [26]. The solar panel cost was \$550 for one 550 W panel from Renogy (model RSP550D-144x2-US) [27].

The membrane cost, spacer cost, and electrode cost were \$75 USD/m^2, \$23 USD/m^2, and \$1200 USD/m^2 [28]. Using this cost model, the capital costs provided predicted a stack cost of \$57,000 USD for a MkIVx600 and \$16,000 for a V20x300. Both stacks are estimated to cost less than the total quoted price for an individual stack. The MkIVx600 quoted cost was \$65,000; 14% greater than modeled. The V20x300 quoted cost was \$21,000; 31% greater than modeled [28]. This discrepancy in cost suggests additional overhead costs associated with the fabrication and assembly of each stack. Although the discrepancy in cost was not uniform between the MkIV and V20, the cost model was adopted. Case study findings presented in Section

4.1 and 4.2 showed the cost advantage of the V20 did not result in lower LCOW.

The following sections adopt an abbreviation to refer to each optimized system and selected operational mode with the following convention: WJ-XY-Z where

- W is the number of serialized stacks.
- X is the operating type; TV for time-variant and F for fixed.
- Y is the operating mode; B for batch, C for continuous, M for mixed.
- Z is the model of stack.

As an example, a specific system that has 3 serialized V20x150 stacks and operates in time-variant, batch mode will have the system abbreviation 3J-TVB-V20x150.

4.1 Potable water in Elmendorf, Texas

The state of Texas has been rapidly increasing desalination capacity over the past several decades. Desalination plants in Texas accounted for 9% of all installed plants in the USA in 2010 rising to 13% of installed plants in 2017 [29]. Increasing desalination capacity is part of the decades-long Texas State Water plan which seeks to combat increasing water scarcity caused by statewide drought and population growth [30]. The 2022 Texas State Water Plan estimates municipal freshwater shortages for each decade through the 2070s. Municipal shortages are expected to grow from 214,613 acre-ft/year (725,000 m^3/day) in the 2020s to 3,144,304 acre-ft/year (10,600,000 m^3/day) in the 2070s. Municipal shortages are estimated to overtake shortages in the irrigation, manufacturing, steam electric power, livestock, and mining sectors in the 2070s [30]. To combat this shortage, Texas plans to employ water reuse, demand reduction, and increased desalination capacity, among other water conservation strategies [30]. 30 new groundwater desalination projects for municipal use are planned across Texas in the 2030s, including new installations and expansions [30], demonstrating Texas' commitment to new desalination infrastructure.

The San Antonio Water System (SAWS) is a municipal water supply with a demonstrated focus on new and expanded desalination capacity, illustrated by the SAWS H2Oaks Center, completed in 2016. The H2Oaks Center is a modern brackish water RO desalination plant with a design capacity of 45,000 m^3/day. The reported utilization in 2020 was 28,000 m^3/day [31]. The facility integrates desalination with aquifer storage and recovery (ASR) as a product water reservoir and deep well injection (DWI) for brine disposal. In February 2021, Winter Storm Uri caused state-wide power outages, including at the H2Oaks Center. SAWS now plans to install backup natural-gas powered backup generators at H2Oaks Center to mitigate the impact of future power outages [32]. Simultaneously, SAWS is working with the local energy utility to evaluate the feasibility to install 80-125 MW of new solar capacity on the land surrounding the H2Oaks Center to reduce the grid reliance and increase energy resilience [32]. These features make the SAWS site an excellent case to explore the

potential for TEDR systems to complement the projected need for desalination in the SAWS municipal water supply, as well as address the need for a desalination technology that pairs well with renewable power sources. This case therefore focuses on Elmendorf, TX where the H2Oaks Center is located.

Case Parameter	Value	Unit
Target Plant Production Rate, $\dot{V}^{p}_{\nu,WTP,target}$	5520	[m^3/day]
Reliability, ν	95	[%]
Feed Concentration, $C_{d,0}$	1400	[ppm NaCl]
Target Concentration $C_{d,S}$	300	[ppm NaCl]
Recovery Ratio, ξ	90	[%]
System Life, m	10	[years]
Interest Rate, k_d	5	[%]
Maximum Pump Efficiency, η^{max}_{pump}	40	[%]
Rated PV Panel Output, P^{rated}_{PV}	550	[W]
Stack Power Supply Efficiency, η_{PS}	80	[%]
Static Pressure Losses, Δp_{loss}	69,000	[Pa]

Table 4.4: Case parameters used in the formulation of the Elmendorf, TX case study.

Functional requirements and case parameters for Elmendorf were derived from the 2022 Texas State Water Plan, the Texas Water Development Board (TWDB) desalination plant database, and insight from stakeholder interviews. Several semi-structured interviews in Texas were conducted in Summer 2023 with a senior analyst at SAWS and two TWDB employees working in the TWDB Innovative Water Technologies department including a Manager and Desalination and Reuse Engineering Specialist. The interviews included questions designed to ascertain the operating requirements of current and future proposed desalination systems as well as pain points of current desalination processes. Key functional requirements of the case derived in part from these interviews are included in Table 4.4.

The average plant size in Texas was 5,300 m^3 when surveyed in 2017 [33]. Twenty of the thirty municipal desalination plants planned in 2030s have a capacity of 6,000

m^3/day or less [30]. The representative WTP capacity for this study was chosen to be 5,520 m^3/day, which is 20% of the actual H2Oaks Center's reported 2020 utilization. The smaller size of this plant reflects a trend toward smaller plants sizes for new desalination plants installed in the 2030s [30]. The feed concentration, product concentration, and recovery ratio were chosen based on the performance of the H2Oaks Center [31]. This reflects a desire to understand whether a TEDR architecture could be beneficial compared to the existing plant, which is based on RO. An irradiance profile for Elmendorf was selected from the National Renewable Energy Laboratory (NREL) National Solar Radiation Database (NSRDB) [34]. The dataset includes the GHI for 2022 near Elmendorf, Texas (Latitude 29.14, Longitude -98.41).

Cost Model	Type	Value
Brine Disposal	OPEX, USD/yr	$G_{brine} = 365(1.1243\dot{V}^{b}_{\nu,sys})$

Table 4.5: The brine disposal cost for Elmendorf, Texas used in the calculation of yearly operating expenses. The 365 multiplier reflects the conversion from daily to yearly cost.

The cost of brine disposal, presented in Table 4.5, was set to the 2024 SAWS monthly wholesale sewer rate [35]. The H2Oaks Center utilizes DWI as it primary brine disposal method. Costs for DWI vary greatly according to the drilling depth and quantity of brine disposed [36]. It was not possible to attain an accurate brine disposal cost for the H2Oaks center for this study. The SAWS municipal sewer rate was selected instead. Although sewer disposal is less prevalent in Texas, it is a common practice in California and Texas, where the greatest proportion of desalination plants in the USA are located [29, 36].

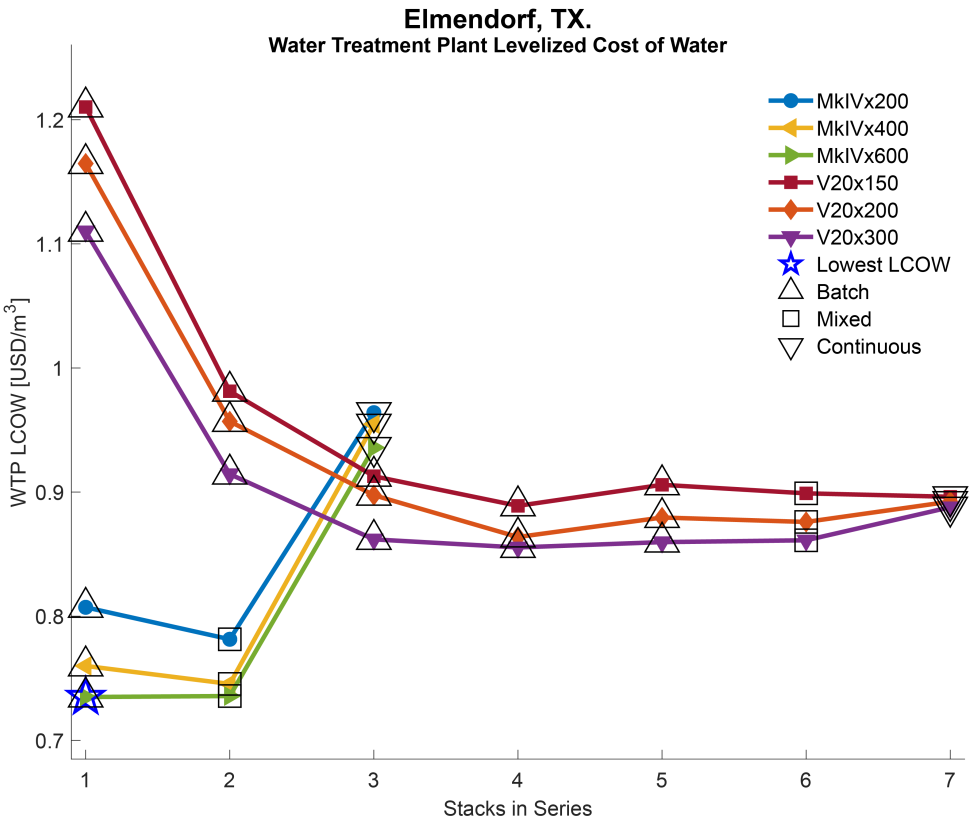

Figure 4-1: Optimization results for potable water in Texas. Each point on the figure represents a cost-optimal WTP system defined by a unique architecture and system configuration. The resulting operating mode and lowest LCOW are indicated. Omitted from this figure is the system type, and mode of operation (fixed or time-variant). All optimal systems were time-variant.

Figure 4-1 presents the WTP LCOW for 30 optimized architectures designed to deliver potable water in Elmendorf, Texas, each capable of meeting the identified needs in Table 4.4. The results are also tabulated in the Appendix in Table A.1. Nine systems utilize MkIV stacks and 21 systems utilize V20 stacks. In addition, the design and performance outcomes of the optimized architectures are presented in Table A.1. The least-cost optimized WTP contains 59 optimized TEDR systems within the WTP. Each system is comprised of one Veolia MkIVx600 EDR stack and

was found to operate in a time-variant batch configuration (1J-TVB-MkIVx600). These results are explored in depth in the following sections.

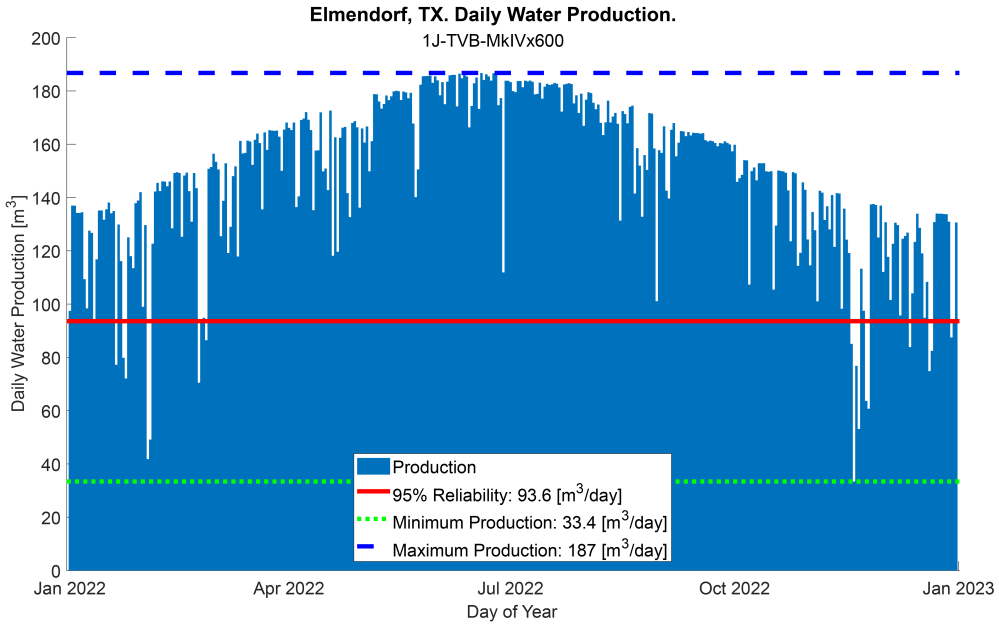

Figure 4-2: Elmendorf, TX 1J-TVB-MkIVx600 daily production for 2022 historical irradiance.

4.1.0.1 Utilization of time-variance

In addition to the least-cost architecture, all of the cost-optimized architectures utilize time-variance ($x_{owl} < x_{owu}$). The model must consider several key trade-offs to determine that time variance is the most optimal configuration. A time-variant system can utilize a larger fraction of solar energy to desalinate water compared to a fixed system but it typically has a higher capital cost to support a power system that is capable of delivering a higher power for desalination and pumping. In addition, the system must weigh the cost of operating at a higher SEC at higher powers. The selection of time-variant operation in every case suggests that the additional water produced by each time-variant system reduced the total number of the systems required to meet the target demand, outweighing the increase in capital cost per system. This

reinforces the net benefits of TEDR operation originally proposed by He et al. [13].

4.1.0.2 Comparison with existing RO

From Table 4.4, the LCOW for the optimized WTP is \$0.7349 USD/m^3. This is less than the reported LCOW for the H2Oaks Center, which is \$0.92/m^3 [37]. Although the LCOW produced by the model is an estimate, this favorable comparison between a plant designed with TEDR systems and the existing RO systems at the H2Oaks Center is promising and suggests that further analysis would be worthwhile to compare these costs in greater detail. Both the optimized LCOW and the reported LCOW of the H2Oaks center are higher than the current residential cost of water in the San Antonio Water System, which is \$0.24 USD/m^3[35]. This suggests that the cost of water for a TEDR system would likely need to be subsidized, similar to the existing H2Oaks facility. It also suggests that the subsidies would be similar in magnitude to existing subsidies.

The model-predicted capital cost of the optimal WTP was \$9,500,000, equivalent to \$1,700 USD per m^3/day of production capacity. In comparison, the reported capital cost of the H2Oaks Center is \$192,000,000, equivalent to \$4,200 USD per m^3/day of production capacity [37]. This difference in capital cost is likely due in part to costs that are included in the H2Oaks Center cost but not considered in the TEDR model, such as the cost of infrastructure, labor, and other capital costs. However, EDR systems are typically reported to have significantly higher capital costs compared to RO, though the LCOW may be lower. The lower projected capital cost suggests that the cost-reducing benefits of TEDR operation may be weighing favorably against RO for this use case.

4.1.0.3 Potential flexibility benefits of TEDR

The daily production volume of the most optimal system, 1J-TVB-MkIVx600, is presented in Figure 4-2. This demonstrates that on most days, the TEDR WTP is delivering significantly more water than the minimum reliable volume of product water. The minimum volume of water delivered in a single day by the WTP is 2,000 m^3

in November, 2022 and the maximum volume is 11,000 m^3 in June, 2022. As a result of this excess capacity, the total annual water production of the optimized TEDR WTP in the modeled year was 3,200,000 m^3, compared to 2,000,000 m^3 required to meet the minimum reliable product water volume target. This extra capacity can significantly impact the LCOW. The optimized LCOW considers only the minimum reliable product water volume target (Equation 2.35), which effectively assumes that any excess production is not valued. Considering the actual annual production rate, the LCOW for the cost-optimal TEDR WTP is \$0.5069 USD/m^3, which is 31% less that the LCOW considering only the minimum reliable product volume. Water produced in excess of demand could feasibly be stored in a holding tank, reservoir, or ASR, which is the current practice of the H2Oaks Center. The water produced in excess could also be used to supplant water production on low irradiance days, reducing the number of systems in the WTP required to achieve the target production rate. This flexibility suggests that the LCOW in practice would be less than the model estimate, making the technology even more favorable compared to the existing RO plant.

4.1.0.4 Architecture trade-offs

Figure 4-1 reveals key trade-offs between different architectures for the Elmendorf, Texas potable water case. The number of cell pairs impacts the WTP LCOW significantly; systems based on the same stack model with fewer cell pairs show a higher LCOW. When the number of cell pairs is lower, the cost per stack cost is reduced because each stack contains less membrane area. However, a consequence of the lower membrane area is an increased flow constriction, a higher pressure drop, and a lower average production rate per stack. The results suggest that stacks with larger number of cell pairs were favored for the Texas case, where the WTP was comprised of 10s-of-systems. This indicates that the cost savings per stack with a lower number of cell pairs does not outweigh the reduced production capacity compared to stacks with more cell pairs.

4.1.0.5 Influence of operating mode

The ratio of total number of passes and the number of stacks in series, S/J, determines whether the operating mode of the system is batch or continuous. The most optimal system of Figure 4-1, 1J-TVB-MkIVx600, has a ratio S/J which ranged from 1.9 at the lowest flow rate to 2.5 at the highest flow rate, indicating that it operates entirely in batch mode. The next lowest cost system, 2J-TVM-MkIVx600, had mixed operation, with a ratio S/J from 1.0 to 1.1, operating in continuous mode for the lowest 40% of its operating range. This outcome is also demonstrated in Figure 4-3, which compares the total attainable salt cut in three cost-optimal MkIV systems to the required salt cut to achieve the desired product water concentration (in this case, 78.5%). The least cost architecture operates in batch mode over its entire operating range, and the second least-cost system operates in batch mode over 40% of its operating range. These results demonstrate that the model is favoring batch operation for the Texas potable water case.

A batch system can vary its power consumption over a wider range to more closely match the available power from the PV array compared to mixed or continuous systems. From Table A.1, the optimal batch system in Elmendorf utilized 57% of the available solar from its PV array, a higher utilization than the next eight lowest cost systems. This reduces the capital cost of a PV system and allows the batch system to benefit more from time-variance than a continuous system. These results suggest that the wide range of power consumption, and flexible operation of the batch system, outweighs other penalties, such as the higher SEC when operating at higher power levels. These results, presented in the Appendix in Table A.1, also suggest that higher solar utilization is favorable in terms of LCOW.

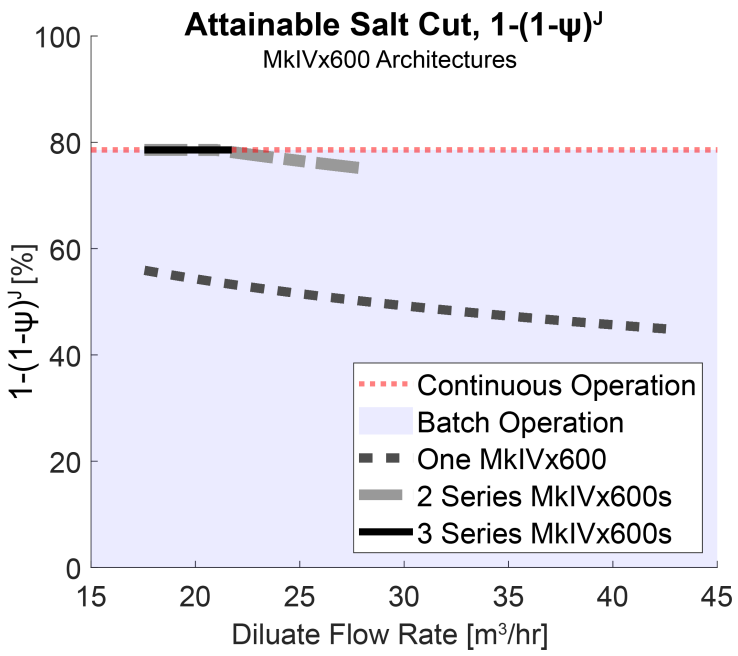

Figure 4-3: The attainble salt cut is a measure of the total salt removed by all stacks during the first pass of operation, or for all $s = j$. When the attainable salt cut is equivalent to the salt cut required to desalinate from the feed to the target concentration, the system operation is continuous. Any system which operates with an attainable salt cut less than salt cut required for continuous operation operates in batch mode. Here, 2 Series MkIVx600 has mixed operation, transitioning from continuous operation to batch operation dependent on the diluate flow rate.

During continuous operation, there is a 1:1 relationship between diluate flow rate and water production rate. A WTP comprised of systems that operate in mixed mode can achieve the same productivity for a similar cost as a batch system, indicated by the small difference in LCOW between the plants comprised of 1J-TVB-MkIVx600 versus 2J-TVM-MkIVx600. The subtlety in this trade-off highlights the need for system designer to be able to consider multiple architectures and system configurations to design cost-optimized systems.

4.1.0.6 Influence of stack model

From Figure 4-1, the larger MkIV stack was favored, generally, over the smaller V20. The shorter flow path of the V20 removes less salt per pass compared to the MkIV. Although the V20 is lower cost, the low product concentration required for potable water favors the MkIV. In addition, the MkIV can be configured with more cell pairs compared to a V20. These results demonstrate that the increase in active membrane area in the MkIV is beneficial for a large, municipal WTP attempting to achieve potable water quality in Texas.

Additional model-specific stack costs such as the number of fittings, the size of length of pipe, or other hardware costs are not considered in the model, though they may affect the trade-off in cost between a MkIV and V20. This analysis demonstrates that a WIP that utilizes V20s may have a higher number of stacks in the WTP compared to the MkIV. The larger number of stacks required for V20 systems will require more fittings and model-specific costs, but the small footprint and light weight of a V20 may also prove valuable if the cost of infrastructure is considered. The model provides a framework that would allow a designer to consider these additional costs.

The number of serialized stacks and the operating mode (batch, mixed, continuous) are closely linked. For the MkIV, fewer serialized stacks operating in batch or mixed modes, tended to be the lowest cost. However, for V20 stacks, the LCOW was highest for the fewest number of serialized stacks, suggesting that the added capital cost of adding more serialized stacks was worthwhile to achieve the higher daily production volume. For the Texas case, the impact of this outcome is that lowest cost systems always selected a number of serialized stacks that resulted in batch operation, as opposed to mixed or continuous. This supports the conclusion that batch systems are favored for time-variant operation when the desired product water concentration is low, as in the potable water Texas case.

4.1.0.7 System configuration trade-offs - lower operating window

Clear trade-offs and trends are apparent for each of the four system configuration design variables - lower operating window, upper operating window, design irradiance level, and BEP. The lower operating window of the most cost optimal system was set at 1.2%. For all 30 optimized systems, the range of the lower operating window was very low - 0.0% to 4.6%. The selection of the lower operating window directly impacts the minimum system power level required to start operation. Regardless of system architecture or operating mode, these results demonstrate that the optimizer favors lower values for the lower operating window. This outcome is consistent with the understanding that TEDR operates with the lowest specific energy consumption (SEC) at the lowest power levels [11]. In addition, when the operating window is low, the minimum system power, P_{sys}^{min}, is correspondingly low. This allows the system to operate for a greater portion of the day, reducing the cost of the system by producing more water during the day. The consistent selection of a low lower operating window suggests that systems capable of operating reliably on low irradiance days are favored when the daily and seasonal variation in irradiance is relatively high, as it is in Elmendorf.

4.1.0.8 System configuration trade-offs - upper operating window

There was more variation in the upper operating window across the 30 optimized architectures. This value ranged from 24% to 99%. The least-cost optimal system selected an upper operating window of 77.8%, indicating that the system is making use of the majority of the architecture-constrained operating window. The variation in the upper operating window suggests that the optimizer is considering two competing design strategies to achieve a low LCOW. One strategy selects a smaller value for the upper operating window, causing the WTP to be comprised of more lower power, lower cost systems. The other strategy selects a larger value for the upper operating window causing the WTP to be comprised of fewer, higher power, higher cost systems. The inconsistency of upper operating window selection suggests that the choice may

depend on the stochastic nature of the GA, reflecting multiple local minima for the optimization. The optimized upper operating window for the top three lowest cost systems were 77.8%, 82%, and 96.6%, respectively. This suggests that the optimizer prioritized fewer, higher-power, higher-cost systems when configuring the large WTP designed for Elmendorf.

This selection highlights a benefit of time variant operation. WTPs which have large required production rates and relatively low product concentration targets are able to use time-variant operation to increase the utilization of solar power, making use of the higher power portion of the system's operation at the expense of a increased SEC. The selection of a large upper operating window in the least-cost systems suggests that this benefit outweighs the penalty caused by a higher SEC.

4.1.0.9 System configuration trade-offs - target solar irradiance level

From Table A.1, the least cost optimal system had a PV array with 157 panels and was designed to deliver its maximum system power (30 kW) at a target irradiance level of 349 W/m^2. When the solar irradiance exceeds 349 W/m^2, the system cannot utilize the additional power made by the PV array to desalinate water. The 157, 550 W panels used in the least-cost optimal system are nominally rated for 86 kW at 1000 W/m^2 - this is 2.9 times greater than the maximum system power consumption. A conventionally-designed PV array would require only 55, 550 W panels to output 30 kW at the conventional design target of 1000 W/m^2. All of the optimized systems in this study selected arrays with a rated power output significantly higher than the maximum power consumption, with arrays rated 2.1 to 6.9 times higher that their power rating. This result may reflect the high frequency of lower irradiance days in the winter and fall in Elmendorf, with the optimizer selecting for systems that can be more productive on lower irradiance days.

System designers must also consider the cost of land and installation for large PV arrays when selecting the optimal system design. Future iterations of the model could incorporate a land cost, or incorporate battery energy storage, to reduce the size of the required PV arrays and consider these trade-offs. If the cost of battery storage is

low, the cost savings of a smaller array size may reduce the LCOW.

4.1.0.10 System configuration trade-offs - BEP

The BEP was placed at 19% system operating window for the least cost optimized system. Over the 30 optimized architectures, the BEP ranged from 0.8% to 70%. The selection of the best efficiency point reflects several key trade-offs. The first trade off is between the capital cost of the pump and the minimum power required to operate the system. The capital cost of the pump is based on the maximum required pumping power. A pump that is most efficient at 0% of the system operating window will contribute to the largest increase in LCOW due to its high power consumption at the high end of the flow rate operating range. However, the minimum power consumption of the system will be low, enabling operation at lower irradiance levels over a longer portion of the day. In contrast, a pump that is most efficient at 100% of the system operating window will have the lowest power consumption and contribute the least to the LCOW, but at the expense of an increase in the minimum power required to operate the system. The increase in minimum required power will cause the system to operate for a shorter portion of the day, ultimately producing less water.

In Elmendorf, the top 23 optimized architectures selected a BEP of 45.2% or less. This suggests that the optimizer is prioritizing more efficient low-power operation for this case. The higher pump cost was amortized by the additional water produced throughout the day, particularly during periods of low irradiance. This trade-off suggests that the irradiance profile of Elmendorf allowed the optimizer to leverage low-power operation.

4.1.0.11 Plant performance considerations

All of the system configuration design variables are constrained by Equation 2.34, which requires the WTP to be comprised of an integer number of systems. In addition, the WTP LCOW is based on delivering only the minimum reliable product water target, set by the functional requirements of the case. If the required daily production of the WTP is not evenly divisible by the reliable daily production of the system, the

net effect is that the WTP must purchase additional capital equipment without the ability to amortize additional production capacity to minimize the LCOW. Any of the four design variables may be tuned, to varying degrees, to achieve a system design which is very close to an integer divisor of the plant demand. In the case of the cost-optimal system in Elmendorf, the daily demand of the WTP is met exactly with 58.98 systems, requiring 59 systems to be installed. This results in 0.3% of the capital cost of the WTP contributing to excess capacity that is not considered in the LCOW. For large WTPs, such as the Elmendorf case, the optimizer can select from a larger array of system configurations that result in an integer number of systems in the WTP, minimizing excess capital cost. This behavior suggests that, as the number of systems in the WTP decreases, the optimizer compromises the performance of the individual systems to favor including an integer number of systems that exactly meet the required production target.

4.1.0.12 Demonstrated utility of the simplified design tool

The findings in Elmendorf illustrate the complexity of the considered trade-offs, particularly for WTPs comprised of 10s-of-systems. These trade-offs are often subtle and related to multiple interacting parameters that would be difficult to assess using a more computationally intensive tool. In the Elmendorf case, the optimizer identified multiple low-cost designs with nearly identical LCOW values (the second least-cost system has an LCOW just 0.11% greater than the least-cost optimal system). Given an array of similarly performing architectures, a system designer could have additional flexibility to select a system based on factors that are not explicitly included in this simplified model. For example, the different total number of stacks among the similar selected architectures may have different maintenance requirements or infrastructure costs. The simplified model enables a designer to understand and consider these nuanced trade-offs.

4.2 Irrigation water in Qena, Egypt

Qena, Egypt is located in the MENA region, the most water-stressed region of the world [38]. The existing supply of freshwater cannot meet rising demand [39] and as a result, most food must be imported [40, 41]. Water sources in the MENA region are rapidly becoming more saline [39, 42, 43, 44] and climate change is expected increase the risk of drought and volatility of the water supply [39, 40]. Egypt is at especially high risk due to its severe water scarcity [45], rapidly increasing population [46], and almost complete reliance on the Nile [47]. An interdisciplinary solution to the increasing water scarcity and food insecurity combines water-efficient, drip irrigation with desalination [7]. This case study focuses on the value proposition of desalination for irrigation but will not consider the impact of co-optimization with a drip irrigation system or controller.

Case Parameter	Value	Unit
Target Plant Production Rate, $\dot{V}^{p}_{\nu,WTP,target}$	68.5	[m^3/day]
Reliability, ν	95	[%]
Feed Concentration, $C^{b}_{d,0}$	2500	[ppm NaCl]
Target Concentration, $C^{b}_{d,S}$	750	[ppm NaCl]
Recovery Ratio, ξ	80	[%]
System Life, m	10	[years]
Interest Rate, k_d	5	[%]
Maximum Pump Efficiency, η^{max}_{pump}	40	[%]
Rated PV Panel Output, P^{rated}_{PV}	550	[W]
Stack Power Supply Efficiency, η_{PS}	80	[%]
Static Pressure Losses, Δp_{loss}	69,000	[Pa]

Table 4.6: Case parameters used in the formulation of the Qena, Egypt case study

Cost Model	Type	Value
Brine Disposal	OPEX, USD/m^3	$G_{brine} = 365(0.4\dot{V}^b_{\nu,sys})$

Table 4.7: The brine disposal cost for Qena, Egypt used in the calculation of yearly operating expenses. The 365 multiplier reflects the conversion from daily to yearly cost.

The relevant case parameters are presented in Table 4.6 and the cost model for brine disposal is presented in Table 4.7. The brine disposal rate was set based on the commercial waste water management rate in Egypt [48]. The targeted daily production was selected based on the maximum crop water requirement for a 5 hectare crop of onions in Qena, Egypt, calculated following methodology outlined by Grant et al. [49]. This region is in near brackish groundwater reserves, but south of the Nile Delta. The calculated maximum daily crop water requirement results in a daily production of 68.5 m^3/day of water. The irradiance profile profile used was selected from the NSRDB for 2019 near Qena, Egypt (Latitude 26.16, Longitude 32.72) [34].

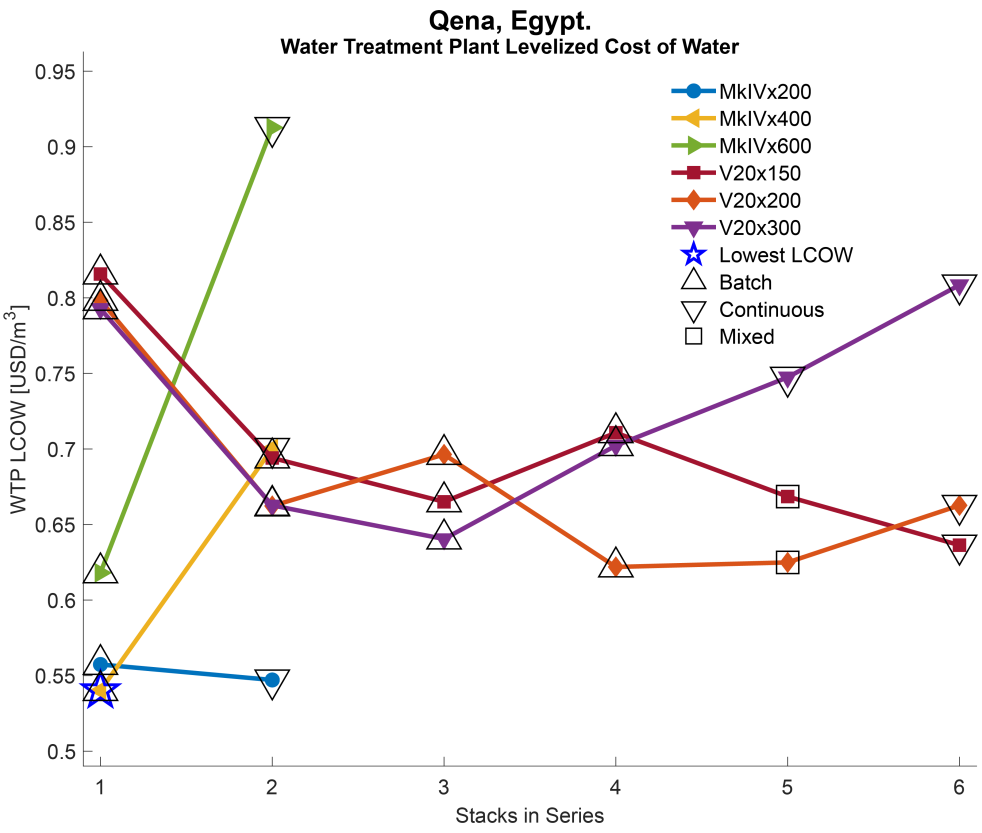

Figure 4-4: Optimization results for irrigation water in Qena, Egypt. Each point on the figure represents a cost-optimal WTP system defined by a unique architecture and system configuration. The resulting operating mode and lowest LCOW are indicated. Omitted from this figure is the system type, and mode of operation (fixed or time-variant). All systems were time-variant, except 2J-FC-MkIVx600 whose operation was fixed.

Figure 4-4 presents the WTP LCOW for 24 optimized architectures designed to deliver desalinated irrigation water in Qena, each capable of meeting the identified needs in Table 4.6.The results are also tabulated in the Appendix in Table A.2. The design and performance outcomes of the optimized architectures are presented in Table A.2. The relatively small size of the WTP and lower desired product water concentration reveal new trade-offs compared to the Elmendorf, Texas case. The

least-cost optimized WTP is comprised of one batch system and has a LCOW of \$0.5402 USD/m^3. The optimized WTP is constructed from one Veolia MkIVx400 which operates in time-variant batch mode (1J-TVB-MkIVx400). The day of lowest production occurred in January, producing 0 m^3. On that day, there was insufficient irradiance to generate the power required to operate the system. The day of highest production occurred in July, producing 125 m^3.

4.2.0.1 Impact of additional water production

The modeled WTP production (based on historical irradiance data from 2019) was 36,700 m^3. Similar to the Elmendorf case, this was far in excess of the 25,000 m^3/year required for reliable operation. If the WTP could amortize its cost based on the full volume of water produced, the resulting WTP LCOW would be \$0.4000 USD/m^3, a 26% cost reduction. This impact on LCOW is similar to Elmendorf, which has a much larger target production volume compared to the Qena case.

The irrigation case offers additional avenues to create value from the excess water production enabled by a time variant system. For example, a farmer might choose to grow an additional crop, allowing them to profit from the additional production capacity.

4.2.0.2 Influence of required salt cut

In the Elmendorf case study, the operating mode and number of serialized stacks was a strong predictor of WTP LCOW. In that case, batch systems comprised of fewer stacks tended to be favorable. The least-cost optimal WTP for the Qena case was consistent with this finding. The ratio S/J for the least-cost optimal system ranged from 1.5 at low powers to 1.8 at higher powers, indicating that the optimal WTP operates in batch mode. However, unlike in Elmendorf, the next lowest LCOW architecture operates as a pure continuous system. This system - 2J-TVC-MkIVx200 - included one system in the WTP, with an LCOW just 1.3% higher than the least-cost optimal WTP. This difference in preferred operating mode likely reflects the lower total required salt cut necessary to achieve the desired product water concentration in

the Qena case. This benefits continuous systems, which have a production rate that scales linearly with the diluate flow rate. This result suggests that the lower pressure drop, lower power requirement, and wider operating range of two MkIV stacks operating continuously is more favorable for small farm irrigation applications compared to the less favorable configuration of three MkIV stacks operating continuously for potable water in Elmendorf.

4.2.0.3 Influence of number of systems in the WTP

Each of the system configuration design variables demonstrated a greater variation between architectures in the Qena case compared to the Elmendorf case. The results from the Elmendorf case suggest that the selection of these design variables may be influenced by the constraint to contain an integer number of systems in the WTP. The optimizer may sacrifice the optimal performance of individual systems to achieve an integer number of systems in the WTP. The higher variation in design variables and the small size of the WTP in Qena suggests the optimizer prioritized the design of the WTP over the optimal performance of the systems within the WTP.

4.2.0.4 System configuration trade-offs - operating window

The operating window of the least-cost optimal system was configured to use 10.2% to 57.1% of the available architecture operating window. The lower operating window ranged from 0.0% to 10.7% for all 24 optimized systems. The upper operating window ranged from 0.0% to 98% for all 24 optimized systems. The large variation suggests the optimizer selected upper and lower bounds on the operating window that balanced low power and high power production to achieve the required WTP production required by the small plant.

4.2.0.5 System configuration trade-offs - BEP

The BEP for the least-cost optimal WTP was 27% of the system operating window. This value reflects similar trade-offs to those demonstrated in the Elmendorf case, suggesting efficient, low power operation benefits the system in spite of its higher

capital cost. The range of BEP was 7.5% to 99.5% for all 24 optimizations. This demonstrated much more variation than the Elmendorf case. This result suggests the BEP is more closely linked to the capital cost and daily production of the individual system compared to Elmendorf. In the Elmendorf case, the BEP value primarily affected the total number of systems installed in the plant. Twenty of the 24 optimized results resulted in a WTP that was comprised of just one or two systems, contributing to the large variation between systems. Other optimal architectures selected pumps that were more efficient near the maximum system power level, reducing the power consumption of the system and capital cost at the expense of operating for a shorter period of the day.

4.2.0.6 System configuration trade-offs - target solar irradiance level

The least-cost optimized system has a PV array with 59 panels designed to deliver the maximum system power, 17 kW, at a target irradiance level of 517 W/m^2. The 59, 550 W panels are nominally rated to deliver 32 kW at 1000 W/m^2, 1.9 times greater than the maximum system power consumption. The ratio of rated PV power to maximum system power consumption ranged from 1.4 to 4.5 for all 24 optimizations. As in Elmendorf, the oversized PV arrays are largely influenced by reliability. The oversized arrays allows the system to operate more reliably on days with low irradiance. Compared to Elmendorf, this ratio was smaller, suggesting the daytime fluctuations and seasonal variations in irradiance in Qena were lower, had a smaller impact on the reliability, and lower impact on the WTP LCOW.

4.2.0.7 Influence of reliability

The reliability requirement demands that the optimized system can produce the desired volume of product water on most days of the year. In reality, crop water demand varies with the solar irradiance. Crops require more irrigation on days with higher irradiance. A more comprehensive reliability metric would evaluate each day's water production against the day's crop water demand. The use of a product water holding reservoir, such as a pond or tank, may also be considered. This would allow the

system to generate water on high irradiance days and utilize on lower irradiance days or in the evening, when the desalination system is inoperable. Incorporating these elements would likely result in a smaller system with a lower LCOW.

4.2.0.8 Influence of system utilization

PV power system utilization plays a key role in determining the WTP LCOW. A typical crop only requires irrigation for a few months of the year prior to harvest. If the desalination system sits idle while no crop is planted, or the water from the desalination system could not otherwise be sold, the WTP LCOW increases. The required size of the system to depends on the highest targeted daily production but the cost of the system is only amortized over the volume of water produced when crops require irrigation. This suggests that the increase in cost could scale with the inverse of utilization.

4.2.0.9 Selection of fixed operation

Unlike Elmendorf, one system out of the 24 optimized systems tabulated in Table 4.6 demonstrates fixed operation rather than time-variant operation. This system - 2J-FC-MkIVx600 - has the highest capital cost and LCOW of all 24 systems. The upper and lower operating range are both set to 0%, suggesting that the optimizer was trying to reduce the capital cost of pumps and pump controllers to compensate for the very high stack cost. Despite its fixed operation, the system produced 46,500 m^3 of water (based on historical irradiance data from 2019), 86% more than required to meet the reliable demand of the WTP (the most of any system). This outcome suggests that the cost of two MkIVx600s cannot be easily amortized for the low WTP production volume found in the Qena case. Although the system is adequately sized to meet the production rate of the WTP, the quantity of membrane area in two MkIVx600 is better applied to larger WTPs. This is further explained by the lower cost of systems which utilize MkIVx400 and MkIVx200 stacks compared to MkIVx600 stacks. The other 23 systems were time-variant which is consistent with prior work that demonstrated the benefits of time-variant systems for irrigation applications [7].

4.2.0.10 Influence of brine management cost

The brine management options and costs for small farmers using desalination systems for irrigation water are not well understood. Prior work suggests that brine management costs can range from \$0.40 USD/m^3 to \$1.80 USD per m^3 of concentrate produced [50, 51, 52]. Considering this wide range of costs, brine disposal could account for between \$2,500 USD/year to \$11,300 USD/year for the least-cost architecture. That amounts to between 4.3% - 19.4% of the WTP capital cost. Incorporating this into the LCOW adjusts the range from \$0.5402 USD/m^3 to \$0.8902 USD/m^3. In Qena, access to wastewater management is less common and the cost of brine disposal may be on the higher end of the range, resulting in a 65% increase in WTP LCOW. This illustrates the need for high-recovery solutions to reduce the volume and cost of brine management.

4.3 Parameter sensitivity

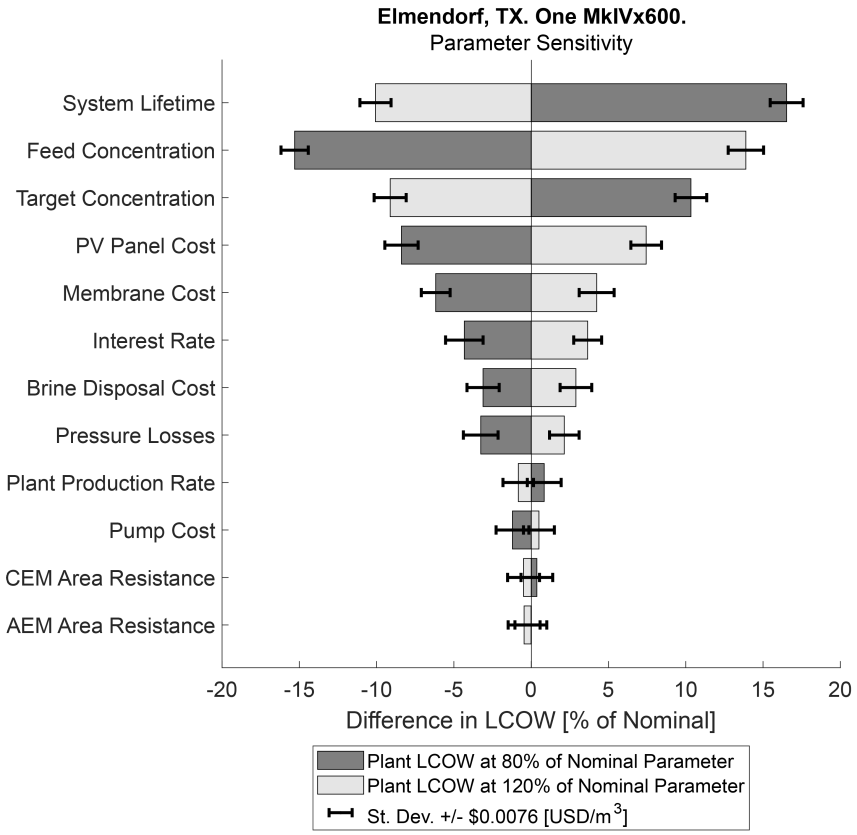

Figure 4-5: Sensitivity to ±20% change in select parameters for the one stack, MkIVx600 system in Elmendorf, Texas. The resulting change in WTP LCOW is reported as a percent of the cost-optimal WTP LCOW from the Elemendorf case study. The standard deviation adopted in Section 2.0.5 is plotted as error bars, indicating change in LCOW that may be attributed to the stochastic nature of the optimizer.

To better identify the cost drivers that result in the greatest change in WTP LCOW, a parameter sensitivity study was conducted, focused on the Elmendorf, Texas case study. Results are presented in Figure 4-5 for the least-cost optimal system - 1J-TVB-MkIV600. The system lifetime, feed concentration, product concentration, PV panel cost, membrane cost, interest rate, brine disposal cost, pressure losses, plant

production rate, pump cost, CEM area resistance, and AEM area resistance were individually varied by ±20% of their nominal values, then the architecture was re-optimized. A sensitivity analysis was also conducted for the least-cost optimal system in the Qena case study - the 1J-TVB-MkIV400. The results for Qena are presented in the Appendix, Section A.

4.3.0.1 Sensitivity to system lifetime and interest rate

System lifetime has the greatest impact WTP LCOW. As the system lifetime increases, the capital cost of the system is amortized over a longer payback period, reflected in a lower capital recovery factor. The LCOW increases as system lifetime decreases for the opposite reason. The interest rate also affects the capital recovery factor. The cost of yearly payments increases with higher interest rates, increasing the LCOW. The impact of interest rate is lower than system lifetime, but illustrates a clear incentive to find the lowest interest loan possible, assuming the capital cost of the system is borrowed from a lender. This finding is consistent for both the Elmendorf and Qena case studies, suggesting that this trade-off holds over a range of size scales and applications.

4.3.0.2 Sensitivity to water concentration

The feed and product water concentration were the two most influential parameters on the LCOW after system lifetime. As the feed water concentration increases, the required number of passes increases, lowering the water production rate of the system. This requires more systems or more powerful systems to be installed in the WTP to achieve the same production. The opposite trend is true for lower feed concentrations. As the desired product water concentration decreases, more passes are required, lowering production rate, and requiring more system or more powerful systems. As the product water concentration increases, the opposite trend occurs. For systems such as in the Elemendorf case, which require high salt removal to achieve the targeted potable water concentration, the impact on LCOW due to changes in concentration is lower. For systems which lower total salt removal, as in the Qena

case, the the impact on LCOW due to changing feed and product concentrations is more pronounced. This suggests that system designers should consider a range of feed and product concentrations that reflect the seasonal fluctuation and years-long variations caused by seasonal changes in the water table due to water extraction, drought, and climate change.

4.3.0.3 Sensitivity to cost model inputs

The capital cost of the PV model for the panels and membranes were the fourth- and fifth-most sensitive parameters. This is consistent with expectations, as these are the two highest-cost components of the system. For systems that have more serialized stacks (not shown in this analysis) the cost of membranes may overtake the cost of PV panels. The cost of the power system, which is due primarily to the PV panels, is a smaller fraction of the LCOW when more serialized stacks are considered. For systems that utilize fewer stacks in series, this suggests that increased emphasis should be placed on the accuracy of the PV cost model inputs. For systems comprised of more stacks in series, the accuracy of the membrane cost model should be emphasized.

The capital cost of the pump has a relatively small impact on the LCOW. This suggests that pump cost is not a major cost driver of LCOW. This impact is likely sensitive to the logarithmic pump cost model adopted for this study.

The sensitivity of LCOW due to changes in brine disposal cost is as expected. The volume of brine produced by the WTP is a function of the WTP production volume and recovery ratio. Nominally, yearly brine disposal costs were only 2.7% of the capital cost of the optimal WTP in Elmendorf, suggesting a low sensitivity to these costs. The slight variation in brine cost did not drastically change the outcome of the optimization.

4.3.0.4 Sensitivity to pressure losses

Pressure losses, Δp_{loss}, had a small but significant effect on LCOW. The impact of higher and lower pressure losses led to higher and lower LCOW, respectively. This slight increase in LCOW illustrates the need for a more accurate hydraulic loss model

due to the impact that pressure drop has on LCOW.

4.3.0.5 Sensitivity to membrane area resistance

AEM and CEM area resistances both had a negligible effect on LCOW. This suggests that significant changes to these values would be required to impact the design of a TEDR system.

4.3.0.6 Sensitivity to reliability

System	95% Reliability	93% Reliability	97% Reliability
MkIVx600, 1 Stack	\$0.7387 [USD/m^3] %	\$0.6926 [USD/m^3] -6%	\$0.8375 [USD/m^3] 13%

Table 4.8: Sensitivity to ±2% change in reliability for the one stack, MkIVx600 system in Elmendorf, Texas. The resulting change in WTP LCOW is reported as a both an absolute change and a percent change of the nominal LCOW reported for the cost-optimal system from the Elemendorf case study - 1J-TVB-MkIVx600.

The 13^{th} parameter considered in the sensitivity analysis is system reliability. This parameter was modulated by ±2%. The resulting change in LCOW is tabulated in 4.8. The change in LCOW ranged from -6% to 13% of the nominal value for a -2% to 2% change in reliability. Reliability is the only parameter whose impact on the LCOW exceeded variation in the parameter, suggesting its effect on LCOW is very significant. This result is consistent with the findings of Bian et al. [6] who found that the cost of optimized EDR systems rose sharply when an increased reliability was demanded. This suggests that system designers should consider the lowest feasible reliability value capable of meeting the functional requirements of the system during design. Future work could consider the impact of adjusting reliability according to demand, enabling a greater portion of the water produced by the system to be used to amortize the capital cost of the system. Future work could also consider whether a target reliability can be achieved through design changes that are not currently considered in this model, such as the inclusion of energy storage or water reservoirs, requiring fewer systems in the WTP.

Chapter 5

Discussion

The model presented in this study proposed simplifications to existing parametric models of TEDR performance. These strategic simplifications resulted in reasonable computation time while still encapsulating key scaling relationships of real systems. System simulations required 10s-of-milliseconds of computation. System optimizations required 60 to 120 seconds per optimized system on consumer-grade computer hardware, satisfying the first objective of the study. The modeled desalination rate and power consumption were found to be in relatively good agreement with experimental data from a real TEDR pilot study. A discrepancy was found between the model predicted hydraulic power and experimental data. This suggests future research could focus on the development of an improved pressure drop model that accounts for additional sources of hydraulic power loss. An improved prediction of pressure drop could improve the predicted hydraulic power requirement of the modeled system, allowing the model to better estimate the production rate and cost of a TEDR system. Any modifications designed to increase accuracy of the modeled performance will have to weigh those changes against potential costs to computational efficiency.

The simplified and computationally efficient model was used to create a system optimization and design tool for TEDR WTPs. This tool utilized four system configuration degrees of freedom to enable the design of TEDR WTPs with the lowest LCOW, satisfying the second objective of the study. The utility of the design tool was then demonstrated across two diverse case studies. Thirty unique architectures

were optimized for a case to desalinate potable water in Elmendorf, Texas. Results of the optimization were compared to against an existing municipal scale RO plant to consider the cost of TEDR as an alternative technology to RO with the potential to meet the rising desalination demand in the American Southwest. Twenty-four TEDR systems were optimized to determine the least-cost optimal system for desalination of irrigation water in Qena, Egypt. This case considered TEDR as a potential solution to address the MENA region's rising water scarcity and food insecurity. The outcomes the cases studies were contextualized with local costs, demonstrating clear advantages of TEDR to reliably deliver water at a comparable cost to existing solutions, such as on-grid RO. The findings suggest that TEDR could be cost-competitive in both applications.

In both cases, the lowest-cost, direct-drive, PV-powered EDR systems were found to be time-variant, consistent with previously published studies [13]. The flexible operation of TEDR enables the production of more water, outweighing the costs of the power system required to power the pumps and desalination. This illustrates the utility of a robust, renewable-powered desalination solution.

Numerous nuanced trade-offs were identified that contribute to the system architecture. The trade-off between smaller V20 EDR stacks and larger MkIV EDR stacks is clearer at high production volumes, when a WTP is comprised of 10s-of-systems. Although the larger MkIV represents a higher cost than a V20, the increase in production from its longer flow path and greater number of cell pairs outweighs the added cost. The utility of serialized stacks and continuous operating modes depends greatly on the amount of salt to be removed, the variability in historical irradiance, and targeted WTP reliability. In both cases studies, an alternate design, comprised of multiple stacks in series was identified, allowing the system designer freedom to choose which system to install based on other design factors like the total number of system and stacks, the capital cost of individual systems, or the infrastructure cost of larger PV arrays.

The selection of the system WPC paired with each architecture followed a number of trends. The optimizer tended to select the lower operating window near the lower

bound of the architecture, enabling a system to operate at lower irradiance levels, for a longer portion of the day, at lower SECs. The selection of the upper operating window reflects the trade-off between the capital cost of individual systems and the number of systems in the WTP. When the upper operating window is low, the optimizer is selecting more, low power, low capital cost systems for the WTP. When the upper operating window is high, the optimizer is selecting fewer, high power, high capital cost systems. The target irradiance level is largely influenced by the reliability of the system and the daily and seasonable variation in irradiance. Most often, the lowest-cost system is paired with a PV array which is rated for at least twice the maximum rated power of the system to achieve reliable operation. The selection of the BEP demonstrates the non-trivial trade-off between the high cost of pumps and the impact on system power level. Pumps which are most efficient at low flow rates also minimize the lower power threshold of the system, allowing the system to operate at lower irradiance levels for a longer portion of the day. However, pumps which are most efficient at their lowest flow rate also have the highest capital cost. The optimizer selects the BEP according to the competing goals of efficient low power operation and pumps which are low capital cost.

The validation of this model is limited to experimental data from a pilot system comprised of one EDR stack operating on a low salinity well. The assumptions utilized in this model, particularly for the efficiency of the stack, will likely limit the range of feed and product concentrations that can be accurately simulated by the model. The addition of multiple stacks in series may compound model inaccuracies. Future work may adopt new model simplifications that improve the accuracy of the predictions made by this model.

Future work is recommended to consider the impact of demand, water holding reservoirs, energy storage, and grid power. A model which incorporates the daily fluctuation and seasonal variation of demand may find the additional water produced by the WTP suffices to meet demand reliably with fewer or lower-cost systems. If demand is met through water held in a reservoir, water generated using energy stored in battery buffer, or using a grid-power interconnect, reliable production would likely

be achieved with fewer systems and lower LCOW than reported in this study. These potential cost-savings warrant additional study.

The system cost model may also be amended to include other factors such as infrastructure cost, the cost of valves and piping, the cost of consumables such as antiscalant, or the added cost to the consumer when considering for-profit operation. Provisions for these added costs could are easily integrated into future iterations of the model.

Chapter 6

Conclusion

This novel TEDR model was demonstrated to be a powerful tool capable of capturing a wide range of applications for TEDR. This tool can enable more robust decision making and reveal non-trivial trade-offs between competing designs. With this model, TEDR system designers can quantify year-long system performance for diverse architectures with minimal computation. This model can help facilitate the dissemination of renewable-powered brackish water desalination, enabling system designers to leverage the unique ability of TEDR systems to adapt to diverse environmental conditions. This design tool can aid in the creation of cost-effective desalination solution that can help address global water scarcity.

Appendix A

Tables

A.0.1 Tabulated optimization results

A.0.1.1 Elmendorf, Texas optimization results

Rank	System Code	$\forall^{p}_{\nu,sys}$ [m^3/day]	$LCOW_{WTP}$ [USD/m^3]	$LCOW_{WTP}$ Difference [USD/m^3, %]	N_{sys}	G^{CAPEX}_{WTP} [USD]	x_{owl}	P^{min}_{sys} [kW]	x_{owu}	P^{max}_{sys} [kW]	x_{ghi}	GHI_{design} [W/m^2]	PV Rating [kW]	PV Size [% P^{max}_{sys}]	x_{bep}
1	1J-TVB-MkIVx600	93.6	\$0.7349/m^3	\$0.0000/m^3, 0.0%	59	\$9,489,673	1.2%	6.45	77.8%	30	33.6%	349	86.4	290%	19%
2	2J-TVM-MkIVx600	145	\$0.7357/m^3	\$0.0008/m^3, 0.1%	38	\$9,501,925	0.3%	12	82%	26.7	21.6%	224	119	450%	19.3%
3	2J-TVM-MkIVx400	98.6	\$0.7454/m^3	\$0.0106/m^3, 1.4%	56	\$9,653,862	0.5%	8.21	96.6%	19.7	23.3%	242	81.4	410%	31.2%
4	1J-TVB-MkIVx400	53.6	\$0.7599/m^3	\$0.0250/m^3, 3.4%	103	\$9,879,200	2.5%	4.52	60.2%	13.4	28.7%	298	45.1	340%	34.4%
5	2J-TVM-MkIVx200	49.3	\$0.7814/m^3	\$0.0465/m^3, 6.3%	112	\$10,213,470	1.2%	4.14	88.7%	9.19	21.3%	221	41.8	450%	32.2%
6	1J-TVB-MkIVx200	25.8	\$0.8072/m^3	\$0.0723/m^3, 9.8%	214	\$10,614,325	1.3%	2.13	45.7%	5.28	23.7%	246	21.5	410%	24.1%
7	4J-TVB-V20x300	64.2	\$0.8554/m^3	\$0.1205/m^3, 16.4%	86	\$11,364,805	3.3%	5.43	78.3%	17.5	30.7%	319	55	310%	34.2%
8	5J-TVB-V20x300	78.9	\$0.8597/m^3	\$0.1248/m^3, 17.0%	70	\$11,431,349	0.3%	6.96	89.5%	19.1	26.4%	274	69.9	370%	45.2%
9	6J-TVM-V20x300	93.6	\$0.8612/m^3	\$0.1263/m^3, 17.2%	59	\$11,454,369	1.2%	7.35	94.6%	22.3	25.5%	265	84.2	380%	19%
10	3J-TVB-V20x300	56.9	\$0.8619/m^3	\$0.1270/m^3, 17.3%	97	\$11,465,604	0.7%	4.07	93.3%	26.3	46.6%	484	54.5	210%	30.1%
11	4J-TVB-V20x200	52.6	\$0.8638/m^3	\$0.1289/m^3, 17.5%	105	\$11,495,415	0%	3.4	97.5%	17.1	30.9%	321	53.4	310%	23.7%
12	6J-TVM-V20x200	71.7	\$0.8759/m^3	\$0.1411/m^3, 19.2%	77	\$11,684,141	0.6%	4.77	98.6%	16.4	21.2%	220	74.8	460%	6.2%
13	5J-TVB-V20x200	52.1	\$0.8795/m^3	\$0.1446/m^3, 19.7%	106	\$11,739,791	0.6%	4.58	86.3%	12.6	26.6%	276	45.7	360%	37.8%
14	7J-TVC-V20x300	113	\$0.8878/m^3	\$0.1529/m^3, 20.8%	49	\$11,869,123	4.6%	7.58	94.9%	21.3	17.3%	180	119	560%	20.8%
15	4J-TVB-V20x150	37.8	\$0.8889/m^3	\$0.1540/m^3, 21.0%	146	\$11,885,989	0.1%	2.45	75.9%	9.52	23.9%	248	38.5	400%	9.3%
16	7J-TVC-V20x200	73.6	\$0.8924/m^3	\$0.1575/m^3, 21.4%	75	\$11,939,600	1.3%	4.72	92.8%	14.8	19.3%	201	74.3	500%	0.8%
17	7J-TVC-V20x150	55.8	\$0.8962/m^3	\$0.1613/m^3, 22.0%	99	\$11,999,834	0%	3.49	96.9%	11.7	20.3%	211	55.6	480%	1.6%
18	3J-TVB-V20x200	40.9	\$0.8975/m^3	\$0.1626/m^3, 22.1%	135	\$12,019,344	0.9%	2.8	95.2%	17.3	38.7%	402	43.5	250%	36.2%
19	6J-TVM-V20x150	52.1	\$0.8990/m^3	\$0.1641/m^3, 22.3%	106	\$12,042,710	0.4%	3.6	88.8%	10.7	19%	197	54.5	510%	12.7%
20	5J-TVB-V20x150	38.1	\$0.9059/m^3	\$0.1710/m^3, 23.3%	145	\$12,150,018	2%	3.28	77.3%	9.53	28%	291	33	350%	1.5%
21	3J-TVB-V20x150	29.8	\$0.9128/m^3	\$0.1779/m^3, 24.2%	185	\$12,257,356	1.2%	1.99	74.4%	9.4	29.1%	302	31.4	330%	23.3%
22	2J-TVB-V20x300	37.8	\$0.9145/m^3	\$0.1796/m^3, 24.4%	146	\$12,283,655	0.3%	2.93	58.9%	14.7	35.8%	372	39.6	270%	28.8%
23	3J-TVC-MkIVx600	131	\$0.9359/m^3	\$0.2010/m^3, 27.4%	42	\$12,617,057	1.3%	11.9	95.6%	19.1	15.7%	163	117	610%	25.6%
24	3J-TVC-MkIVx400	89	\$0.9547/m^3	\$0.2198/m^3, 29.9%	62	\$12,909,225	2.5%	8.38	97%	12.1	14%	145	83.6	690%	69.7%
25	2J-TVB-V20x200	25.4	\$0.9570/m^3	\$0.2221/m^3, 30.2%	217	\$12,944,562	0%	1.84	39.8%	6.29	20.9%	217	29.2	460%	12.3%
26	3J-TVC-MkIVx200	44.2	\$0.9640/m^3	\$0.2291/m^3, 31.2%	125	\$13,053,714	0.2%	3.86	95.3%	6.58	16.5%	171	38.5	580%	2.5%
27	2J-TVB-V20x150	19.3	\$0.9813/m^3	\$0.2464/m^3, 33.5%	286	\$13,322,617	0.1%	1.39	42.4%	5.06	22.2%	231	22	430%	13.4%
28	1J-TVB-V20x300	17.8	\$1.1101/m^3	\$0.3752/m^3, 51.1%	310	\$15,327,715	0.2%	2.11	30%	6.52	26%	270	24.2	370%	67.7%
29	1J-TVB-V20x200	11.3	\$1.1647/m^3	\$0.4298/m^3, 58.5%	490	\$16,176,603	0%	1.29	23.5%	3.68	23.9%	248	14.9	400%	31.3%
30	1J-TVB-V20x150	9.91	\$1.2103/m^3	\$0.4754/m^3, 64.7%	557	\$16,885,660	0%	1.05	36.9%	4.18	28.2%	293	14.3	340%	58.1%

Table A.1: Optimization results for potable water production in Elmendorf, TX.

A.0.1.2 Qena, Egypt optimization results

Rank	System Code	$\forall^{p}_{\nu,sys}$ [m^3/day]	$LCOW_{WTP}$ [USD/m^3]	$LCOW_{WTP}$ Difference [USD/m^3, %]	N_{sys}	G^{CAPEX}_{WTP} [USD]	x_{owl}	P^{min}_{sys} [kW]	x_{owu}	P^{max}_{sys} [kW]	x_{ghi}	GHI_{design} [W/m^2]	PV Rating [kW]	PV Size [% P^{max}_{sys}]	x_{bep}
1	1J-TVB-MkIVx400	68.5	\$0.5402/^{3}	\$0.0000/m^3, 0%	1	\$84,976	10.2%	7.55	57.1%	16.7	48.3%	517	32.5	194%	27%
2	2J-TVC-MkIVx200	68.5	\$0.5471/^{3}	\$0.0070/m^3, 1.29%	1	\$86,323	1.5%	4.75	94.4%	11.2	27.6%	295	38	340%	51.4%
3	1J-TVB-MkIVx200	34.2	\$0.5574/^{3}	\$0.0172/m^3, 3.19%	2	\$88,301	1%	3.16	41.9%	6.72	41.5%	444	15.4	229%	21.9%
4	1J-TVB-MkIVx600	68.5	\$0.618/^{3}	\$0.0779/m^3, 14.4%	1	\$100,010	0.8%	9.45	13.4%	11.6	35.2%	377	31.4	270%	94.8%
5	4J-TVB-V20x200	68.5	\$0.6219/^{3}	\$0.0818/m^3, 15.1%	1	\$100,762	2.9%	6.28	82.1%	17.2	36.7%	393	44	256%	40%
6	5J-TVM-V20x200	68.5	\$0.6249/^{3}	\$0.0848/m^3, 15.7%	1	\$101,341	3.4%	6.59	53.8%	13.2	33.7%	361	36.9	278%	90.5%
7	6J-TVC-V20x150	68.5	\$0.6363/^{3}	\$0.0962/m^3, 17.8%	1	\$103,543	9.1%	5.11	97.6%	13.8	28.6%	306	45.1	327%	61.7%
8	3J-TVB-V20x300	68.5	\$0.6404/^{3}	\$0.1003/m^3, 18.6%	1	\$104,333	5.2%	7.14	39.9%	12.8	27%	289	44.6	348%	64.6%
9	2J-TVB-V20x200	34.2	\$0.6623/^{3}	\$0.1221/m^3, 22.6%	2	\$108,555	0%	2.87	43.4%	9.44	40.7%	435	22	233%	7.5%
10	2J-TVB-V20x300	68.5	\$0.6627/^{3}	\$0.1225/m^3, 22.7%	1	\$108,628	0.6%	4.8	82.2%	29.1	46.9%	502	58.3	201%	40.8%
11	6J-TVC-V20x200	68.5	\$0.6627/^{3}	\$0.1225/m^3, 22.7%	1	\$108,631	0.5%	6.26	77%	14.2	38.6%	413	34.7	244%	97.4%
12	3J-TVB-V20x150	34.2	\$0.665/^{3}	\$0.1249/m^3, 23.1%	2	\$109,085	10.1%	3.94	48.8%	7.45	33.5%	358	20.9	281%	53.5%
13	5J-TVM-V20x150	68.5	\$0.6685/^{3}	\$0.1283/m^3, 23.8%	1	\$109,754	0.3%	4.7	81.1%	13	21.1%	226	57.8	444%	60.7%
14	2J-TVB-V20x150	22.8	\$0.6941/^{3}	\$0.1539/m^3, 28.5%	3	\$114,687	1.9%	2.29	32.7%	5.38	36.6%	392	13.8	256%	9%
15	3J-TVB-V20x200	34.2	\$0.6964/^{3}	\$0.1562/m^3, 28.9%	2	\$115,134	1%	4.27	24.4%	6.66	36.9%	395	17.1	256%	49.3%
16	2J-TVC-MkIVx400	68.5	\$0.7004/^{3}	\$0.1602/m^3, 29.7%	1	\$115,905	10.7%	9.82	48.9%	14.7	48.3%	517	28.6	195%	28.4%
17	4J-TVB-V20x300	68.5	\$0.7022/^{3}	\$0.1621/m^3, 30%	1	\$116,264	5%	9.97	86.3%	25.8	68.6%	734	35.2	136%	55.6%
18	4J-TVB-V20x150	34.2	\$0.7108/^{3}	\$0.1706/m^3, 31.6%	2	\$117,912	4.7%	4.73	30.7%	6.58	33.2%	355	18.7	284%	65.6%
19	5J-TVC-V20x300	68.5	\$0.7474/^{3}	\$0.2073/m^3, 38.4%	1	\$124,995	10.4%	10.6	35.8%	16	42.7%	457	35.2	220%	54.4%
20	1J-TVB-V20x300	22.8	\$0.7927/^{3}	\$0.2526/m^3, 46.8%	3	\$133,741	1.3%	2.96	12.4%	4.61	20.6%	220	20.9	454%	99.5%
21	1J-TVB-V20x200	17.1	\$0.7984/^{3}	\$0.2582/m^3, 47.8%	4	\$134,823	3.2%	2.12	23.5%	4.83	30.6%	327	14.9	308%	25.8%
22	6J-TVC-V20x300	68.5	\$0.8085/^{3}	\$0.2683/m^3, 49.7%	1	\$136,781	4.8%	9.26	59.4%	18	55.6%	595	30.3	168%	72.6%
23	1J-TVB-V20x150	13.7	\$0.8158/^{3}	\$0.2756/m^3, 51%	5	\$138,183	1.1%	1.45	29.8%	4.51	36.7%	393	11.6	256%	29.4%
24	2J-FC-MkIVx600	68.5	\$0.9127/^{3}	\$0.3726/m^3, 69%	1	\$156,903	0%	12.9	0%	12.9	36.9%	395	33	256%	80.4%

Table A.2: Optimization results for irrigation water production in Qena, Egypt.

A.0.2 Additional validation figures

Figure A-1 contains validation plots whose data is for first pass desalination power, complementing Section 3.

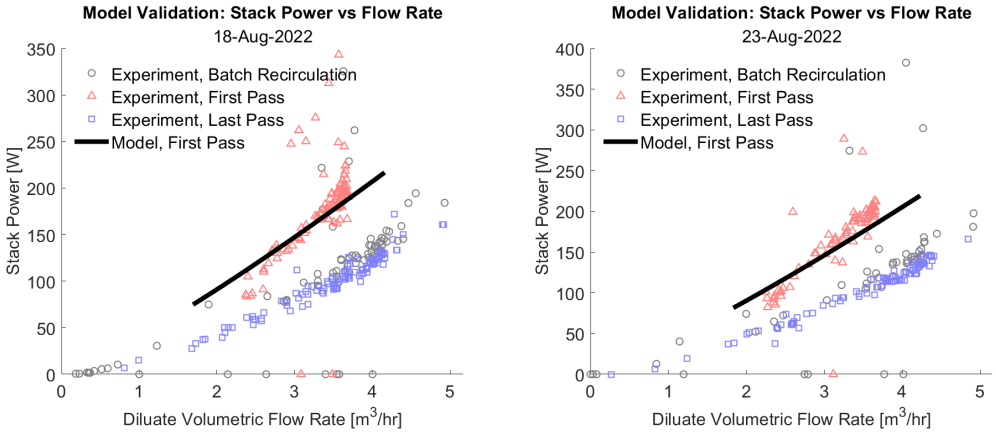

(a)

(b)

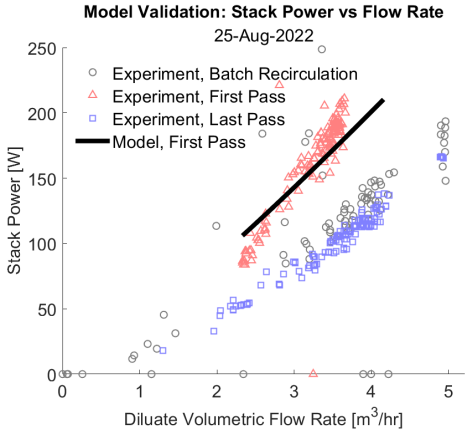

(c)

Figure A-1: Modeled versus experimental desalination power for multiple days of operation of a pilot TEDR system. The first pass occurs during the filling state, distinguished as red triangles. During the first pass, the experiment was drawing water in from the feed source through the stack and into the recirculation tanks. The modeled desalination power has good agreement first pass power.

Figure A-2 contains validation plots whose data is for hydraulic power, complementing Section 3.

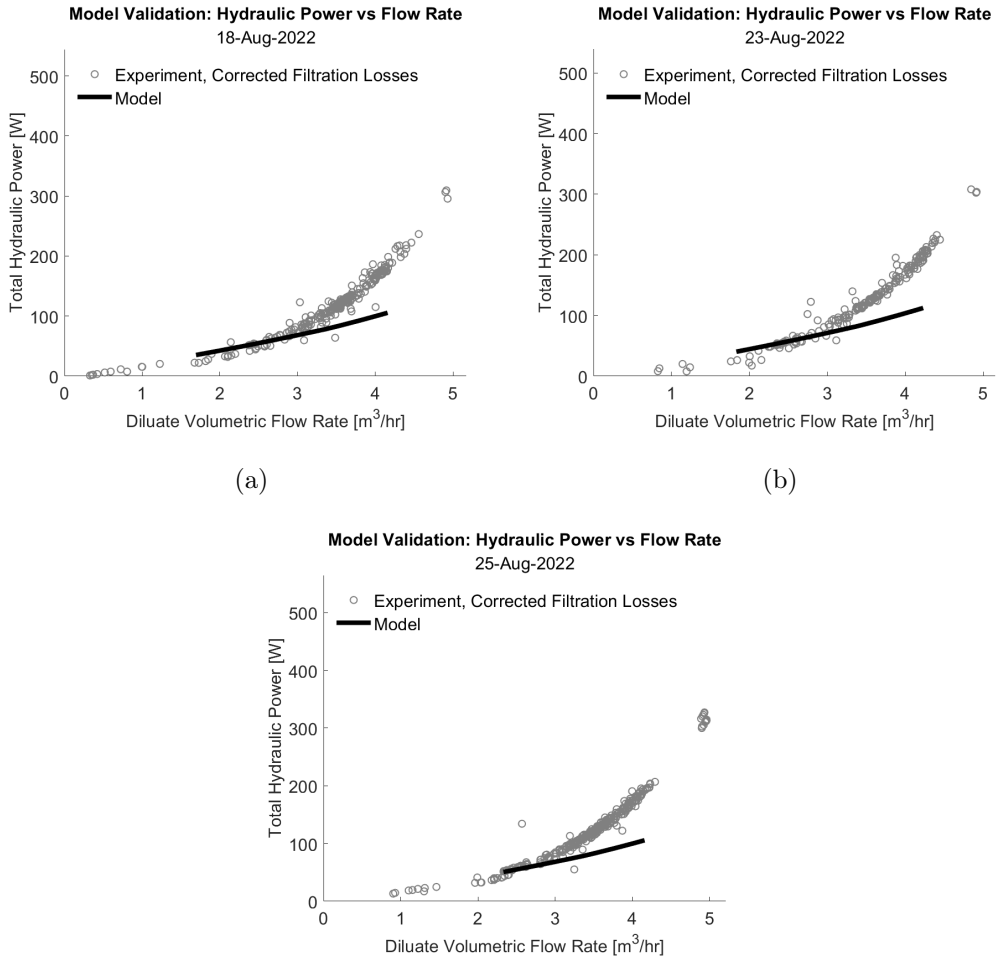

Figure A-2: Modeled versus experimental hydraulic power versus diluate flow rate for multiple days of operation for a pilot TEDR system. The experimental data has one correction factor to account for higher-than-expected filtration losses. As volumetric flow rate increases, the modeled hydraulic power is less accurate suggest there are other losses in the system not accounted for in the model.

Figure A-3 contains validation plots whose data is for product volume, complementing Section 3.

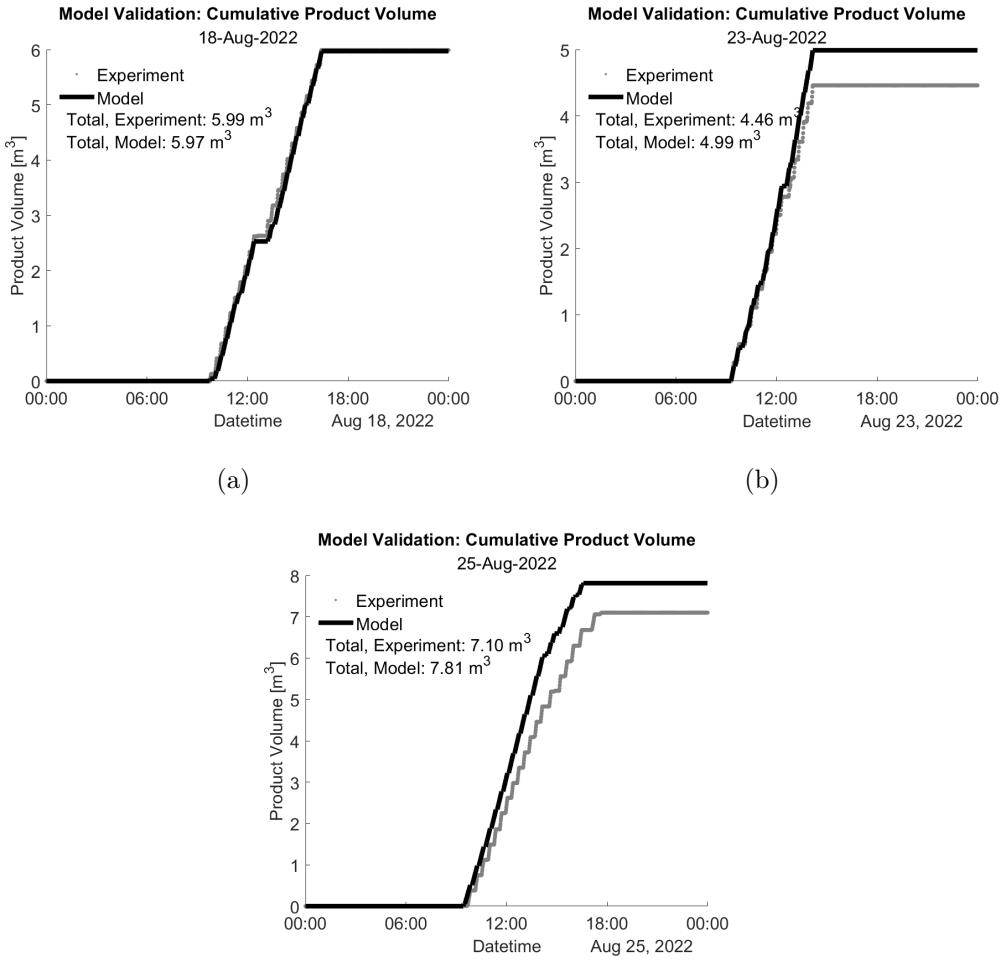

Figure A-3: Modeled and experimental cumulative water production versus time for multiple days of operation of a pilot TEDR system.

A.0.3 Parameter sensitivity for Qena

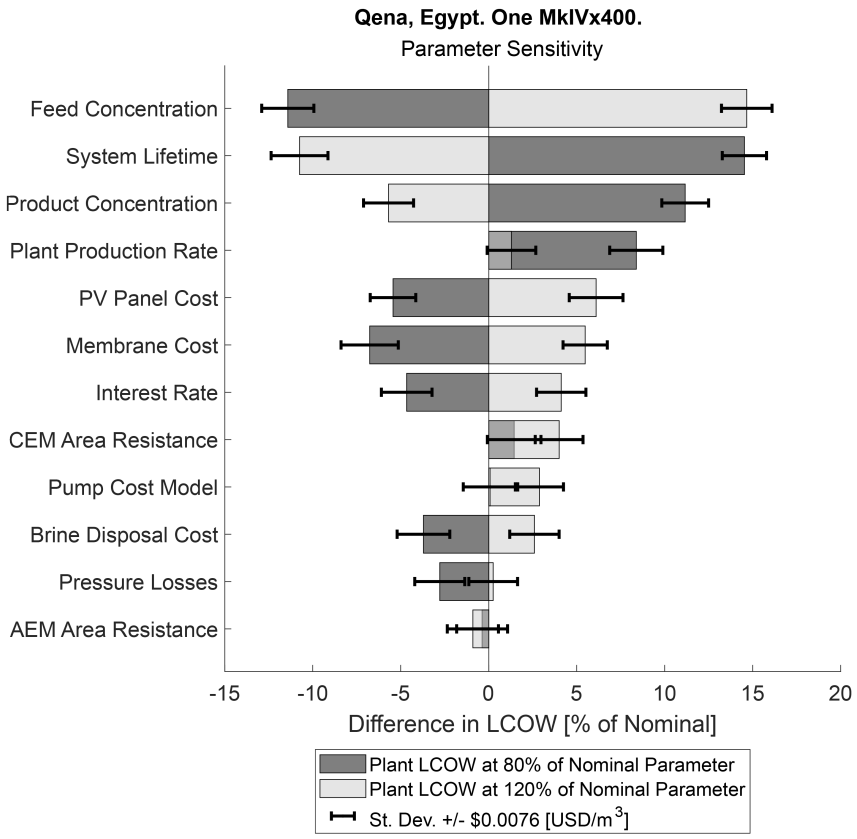

Figure A-4: Sensitivity to ±20% change in select parameters for the one stack, MkIVx400 system in Qena, Egypt. The resulting change in WTP LCOW is reported as a percent of the nominal LCOW reported for the cost-optimal system from the Qena case study, 1J-TVB-MkIVx400. The standard deviation adopted in Section 2.0.5 is plotted as error bars, indicating the change in LCOW that may be attributed to the stochastic nature of the optimizer.

- Feedwater Concentration

  Higher feed water concentration require more passes the remove additional salt, resulting in less daily production, and higher LCOWS. For Qena, which did not require a high level of salt removal for the irrigation of crops, the impact of feed concentration on the LCOW was higherst, among the other 11 parameters

presented in Figure A-4.

- System Lifetime

  The capital recovery factor, crf, increases for shorter system lifetimes, resulting in higher LCOW. The opposite is true for longer system lifetime. In Qena, this trend was found to match the Elmendorf case, suggesting the size of the WTP or the required salt cut does not significantly influence the sensitivity to system lifetime.

- Product Water Concentration

  Higher product water concentrations relax the requirement for the quantity of salt removed, resulting in fewer passes, higher daily production, and a lower levelized cost of water. For Qena, where the initial salt cut was low of irrigation, the resulting change in LCOW reflect the large impact on the LCOW. The opposite trend is true for higher product water concentrations.

- Plant Production Rate

  In both cases, whether the plant production rate increased or decreased, the LCOW was found to increase slightly. When the WTP is small, comprised of just one or two systems, as in Qena, the optimizer may struggle to find a system configuration whose reliable daily production is an integer divisor of the production rate. This impact is less for WTPs which are comprised of more systems. System designers may consider increasing or decreasing the number of cell pairs in the stack to better align the produtivity of the system with the productivity of the WTP.

- PV Panel Cost

  As the cost of PV panels rises and falls, the LCOW has a corresponding increase and decrease, matching the trend of Elmendorf. This suggest the impact of PV panel cost is the same trend across size scales and required salt removal rates.

- Membrane Cost

  Membranes and PV panels typically incur the highest cost in the CAPEX of the

system. As in Elmendorf, the LCOW increases and decreases corresponding to the increase and decrease in membrane cost, suggesting the trend is the same across size scales and required salt removal rates.

- Interest Rate

  Interest rates affect the payments required to amortize the capital cost of the system. Increased interest rates result in higher LCOW. This trend matches expectations in both case studies.

- CEM Area Resistance

  The area resistance of the CEM was found to have little effect when decreased, within one standard deviation of the nominal case. The sharper increase in LCOW for increasing CEM area resistance suggests the increased power requirements had an unexpectedly high impact on the LCOW. Future work is recommended to verify this result.

- Pump Cost Model

  The impact on LCOW from changes in the pump cost model were insignificant for reduced pump costs. The increase in LCOW for increased pump cost was noteworthy. This, again, bears verification with additional analysis, which has not been covered in this study. The results suggest smaller systems are disproportionately affected by higher pump costs.

- Brine Disposal Cost

  For a WTP with a fixed production, the increase and decrease in brine disposal cost has a corresponding increase and decrease in LCOW, matching the ELmendorf case. This suggests the trend holds across size scales and salt removal rates.

- Pressure Losses

  Decreasing pressure losses resulted in a notable change in LCOW, approximately to the same degree as in Elmendorf. Across size scales, there is incentive to

reduce pressure losses in the system which reduce the cost of the power system and correspondingly reduce the LCOW.

- AEM Area Resistance

  The area resistance of the AEM was not found to significantly impact the LCOW.

System	95% Reliability, Nominal	93% Reliability	97% Reliability
MkIVx400, 1 Stack	\$0.5276 [USD/^{3}] 0%	\$0.5154 [USD/^{3}] -2%	\$0.5534 [USD/^{3}] 5%

Table A.3: Sensitivity to ±2% change in reliability for the one stack, MkIVx400 system in Qena, Egypt. The resulting change in WTP LCOW is reported as a both an absolute change and a percent change of the nominal LCOW reported for the cost-optimal system from the Qena case study - 1J-TVB-MkIVx400.

- Reliability

  Similar to the Elmendorf case, the magnitude of change in LCOW, -2% to 5%, exceeded the magnitude of the change in reliability, -2% to 2%. However, compared to Elmendorf, the impact was less. This result suggest the smaller WTP is impacted less by the change in reliability, generally. Or, the result suggest the lower variation in the historical irradiance data in Qena was less, resulting fewer days of unreliable operation within the bounds of 93% and 97% reliability, resulting in a smaller impact on LCOW.

A.0.4 "Last Pass" mathematics

Throughout this study, the "first pass" is used to estimate the desalination power required for the TEDR process, first in the preparation of the WPC, then again as part of the simulation of TEDR performance. The first pass following the convection $s = j$. The "last pass" was also considered for this study as an estimation for stack power. The last pass is derived as $s = j+(S-J)$. One may also consider the "average pass" which considers the average desalination power of the first and last pass for each flow rate, Q_d.

It is possible to evaluate each equation presented in this model which has a dependence s and j for either the first pass, $s = j$, or the last pass, $s = j + (S - J)$. The only equation with an exclusive dependence on the last pass is the calculation of stack inlet and outlet salinities

$$C_{d,s-1} = \frac{C_{product}}{(1-\psi_0)^j} \text{ for all } s = j + (S - J) \tag{A.1}$$

The complement to this is Equation 2.10. In Equation 2.10, the concentrations at the inlet and outlet of each stack are related by salt cut and the feed water concentration. Equation A.1 relates the inlet and outlet concentration to the product water concentration.

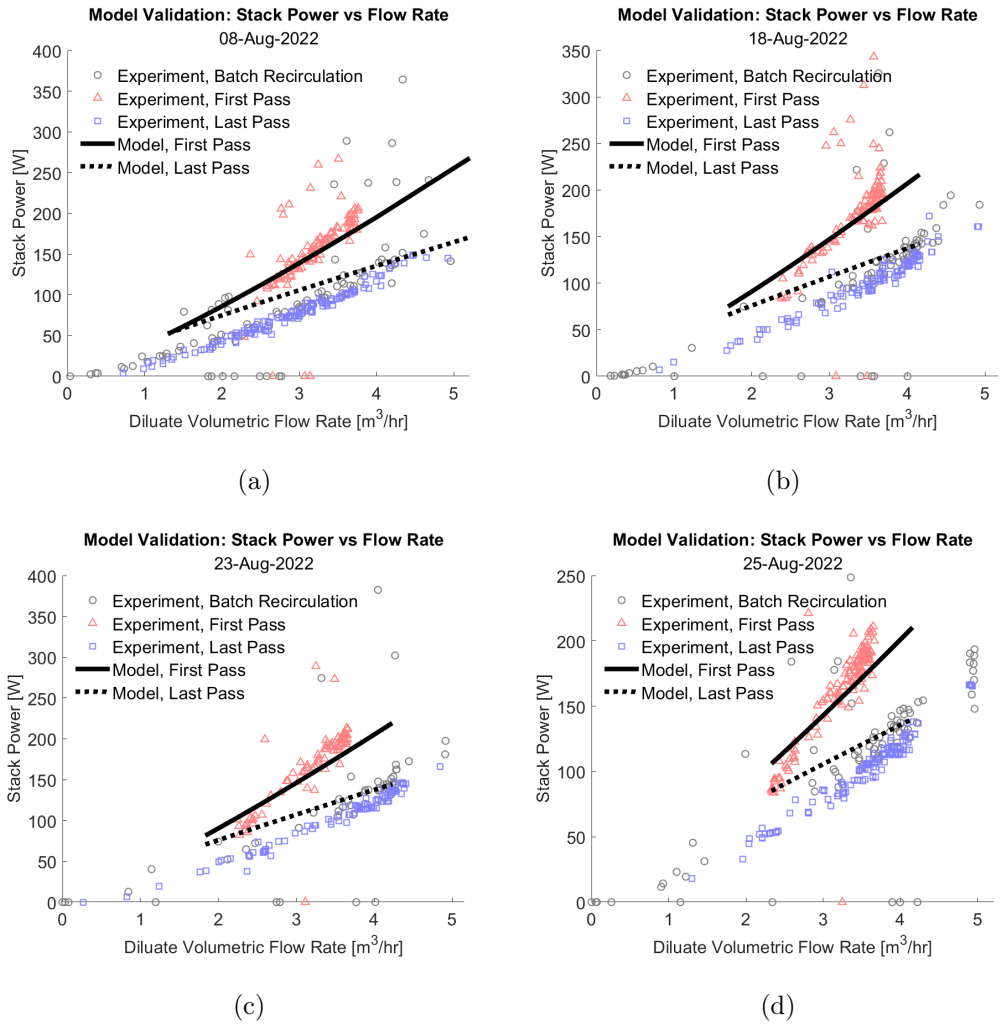

Figure A-5: Modeled versus experimental desalination power for multiple days of operation of a pilot TEDR system. The first pass occurs during the filling state, distinguished as red triangles. During the first pass, the experiment was drawing water in from the feed source through the stack and into the recirculation tanks. The last pass occurs during the draining state, distinguished by blue squares. During the last pass, the experiment was dispensing through the stack and to the product outlet . The modeled first pass desalination power has good agreement. The modeled last pass desalination has somewhat worse agreement which suggest the model inaccuracies caused by the assumed stack efficiency of 100% are greatest toward the end of batch operation. This trend matches expectations.

Bibliography

[1] Veolia Water Technologies Electrodialysis Reversal (EDR), 2024. URL https://www.watertechnologies.com/products/electrodialysis-reversal-edr.

[2] Nirajan Dhakal, Sergio G. Salinas-Rodriguez, Jamal Hamdani, Almotasembellah Abushaban, Hassan Sawalha, Jan C. Schippers, and Maria D. Kennedy. Is Desalination a Solution to Freshwater Scarcity in Developing Countries?, 4 2022. ISSN 20770375.

[3] A. Campione, L. Gurreri, M. Ciofalo, G. Micale, A. Tamburini, and A. Cipollina. Electrodialysis for water desalination: A critical assessment of recent developments on process fundamentals, models and applications, 5 2018. ISSN 00119164.

[4] H. Strathmann. Electrodialysis, a mature technology with a multitude of new applications. *Desalination*, 264(3):268–288, 12 2010. ISSN 00119164. doi: 10.1016/j.desal.2010.04.069.

[5] Roger Sathre, Sai Madhavi, Michela Catena, and Shashi Buluswar. TECHNOLOGY BREAKTHROUGHS FOR GLOBAL WATER SECURITY A deep dive into South Asia. Technical report, 2018. URL www.transformativetechnologies.orghttps://transformativetechnologies.org/insights/water-security/technology-breakthroughs-for-global-water-security-a-deep-dive-into-south-asia/.

[6] David W. Bian, Sterling M. Watson, Natasha C. Wright, Sahil R. Shah, Tonio Buonassisi, Devarajan Ramanujan, Ian M. Peters, and Amos G. Winter. Optimization and design of a low-cost, village-scale, photovoltaic-powered, electrodialysis reversal desalination system for rural India. *Desalination*, 452:265–278, 2 2019. ISSN 00119164. doi: 10.1016/j.desal.2018.09.004.

[7] Jacob N Easley and Amos G Winter. Feasibility and Design of Solar-Powered Electrodialysis Reversal Desalination Systems for Agricultural Applications in the Middle East and North Africa. Technical report. URL https://doi.org/10.1016/j.desal.2023.116628.

[8] Suhaib M. Alawad, Ridha Ben Mansour, Fahad A. Al-Sulaiman, and Shafiqur Rehman. Renewable energy systems for water desalination applications: A comprehensive review. *Energy Conversion and Management*, 286:117035, 6 2023. ISSN 01968904. doi: 10.1016/j.enconman.2023.117035.

[9] Victor D'Amato, Jeff Moeller, and Elizabeth Striano. A new tool for sustainable water management Rethinking decentralized systems. Technical report, 2011.

[10] Tianyi Luo. These 20 Water-Stressed Countries Have the Most Solar and Wind Potential, 5 2018. URL https://www.wri.org/insights/these-20-water-stressed-countries-have-most-solar-and-wind-potential.

[11] Wei He, Anne-Claire Le Henaff, Susan Amrose, Tonio Buonassisi, Ian Marius Peters, and Amos G. Winter. Flexible batch electrodialysis for low-cost solar-powered brackish water desalination. *Nature Water*, 2(4):370–379, 3 2024. doi: 10.1038/s44221-024-00213-w.

[12] Wei He, Susan Amrose, Natasha C. Wright, Tonio Buonassisi, Ian M. Peters, and Amos G. Winter. Field demonstration of a cost-optimized solar powered electrodialysis reversal desalination system in rural India. *Desalination*, 476, 2 2020. ISSN 00119164. doi: 10.1016/j.desal.2019.114217.

[13] Wei He, Anne-Claire Le Henaff, Susan Amrose, Tonio Buonassisi, Ian Marius Peters, and Amos G. Winter. Voltage- and flow-controlled electrodialysis batch operation: Flexible and optimized brackish water desalination. *Desalination*, 500:114837, 3 2021. ISSN 00119164. doi: 10.1016/j.desal.2020.114837.

[14] Natasha C. Wright, Sahil R. Shah, Susan E. Amrose, and Amos G. Winter. A robust model of brackish water electrodialysis desalination with experimental comparison at different size scales. *Desalination*, 443:27–43, 10 2018. ISSN 00119164. doi: 10.1016/j.desal.2018.04.018.

[15] Jonathan Bessette, Shane Pratt, and Amos G Winter. Renewable desalination without energy storage: direct-drive photovoltaic electrodialysis via flow-commanded current control (in press). *Nature*, 2024.

[16] Sahil R. Shah, Natasha C. Wright, Patrick A. Nepsky, and Amos G. Winter. Cost-optimal design of a batch electrodialysis system for domestic desalination of brackish groundwater. *Desalination*, 443:198–211, 10 2018. ISSN 00119164. doi: 10.1016/j.desal.2018.05.010.

[17] Jimmy Tran. *Mapping the Electrodialysis Architecture Design Space by Determining Optimal System Configurations for Different Production Outputs*. PhD thesis, MassachusettsInstituteofTechnology, 2023.

[18] Sahil R. Shah, Sandra L. Walter, and Amos G. Winter. Using feed-forward voltage-control to increase the ion removal rate during batch electrodialysis desalination of brackish water. *Desalination*, 457:62–74, 5 2019. ISSN 00119164. doi: 10.1016/j.desal.2019.01.022.

[19] Francesco Nicolò Ponzio, Alessandro Tamburini, Andrea Cipollina, Giorgio Micale, and Michele Ciofalo. Experimental and computational investigation of heat transfer in channels filled by woven spacers. *International Journal of Heat and Mass Transfer*, 104:163–177, 1 2017. ISSN 00179310. doi: 10.1016/j.ijheatmasstransfer.2016.08.023.

[20] American Water Works Association. American Water Works Association Manual M38. Technical report, 1999.

[21] Walter Richardson, David Cañadillas, Ariana Moncada, Ricardo Guerrero-Lemus, Les Shephard, Rolando Vega-Avila, and Hariharan Krishnaswami. Validation of all-sky imager technology and solar irradiance forecasting at three locations: NREL, San Antonio, Texas, and the Canary Islands, Spain. *Applied Sciences (Switzerland)*, 9(4), 2 2019. ISSN 20763417. doi: 10.3390/app9040684.

[22] John Lienhard, Mohamed A. Antar, Amy Bilton, Julian Blanco, and Guillermo Zaragoza. SOLAR DESALINATION. *Annual Review of Heat Transfer*, 15(15):277–347, 2012. ISSN 1049-0787. doi: 10.1615/AnnualRevHeatTransfer.2012004659.

URL http://www.dl.begellhouse.com/references/5756967540dd1b03,6a1e673c1ba053bf,27f92c3a6df3a77d.html.

[23] Grainger Online Catalog, 6 2024. URL https://www.grainger.com/.

[24] Automation Direct, 6 2024. URL https://www.automationdirect.com/.

[25] Digikey, 6 2024. URL https://www.digikey.com/.

[26] United State Plastic Corporation, 6 2024. URL https://www.usplastic.com/.

[27] Renogy, 6 2024. URL https://www.renogy.com.

[28] Email Conversation between MIT Global Engineering and Research Center and Veolia Water Technologies, 2 2023.

[29] Mickley and Associates. Desalination and Water Purification Research and Development Program Report No. 207. Technical report, 2018. URL https://www.usbr.gov/research/dwpr/DWPR_Reports.html.

[30] Brooke T. Paup and Kathleen Jackson. 2022 State Water Plan, Water For Texas. Technical report, Texas Water Development Board (TWDB). URL www.twdb.texas.govhttps://www.twdb.texas.gov/waterplanning/swp/2022/index.asphttps://www.texasstatewaterplan.org/statewide.

[31] Texas Water Development Board. Texas Groundwater Data Viewer. URL https://www3.twdb.texas.gov/apps/waterdatainteractive/GroundwaterDataViewer/?map=desal.

[32] Julia Murphy. Alamo Area Priority Climate Action Plan. Technical report. URL https://www.epa.gov/system/files/documents/2024-02/alamo-area-5d-02f39101-0-pcap.pdf.

[33] Michael Mickley and Associates. Updated and Extended Survey of U.S. Municipal Desalination Plants. Technical report, 2018. URL https://www.usbr.gov/research/dwpr/DWPR_Reports.htmlhttps://www.usbr.gov/research/dwpr/DWPR_Reports.html.

[34] National Renewable Energy Laboratory National Solar Radiation Database. URL https://nsrdb.nrel.gov/.

[35] 2024 San Antionio Water System Wholesale Sewer Rates, 6 2024. URL https://www.saws.org/service/water-sewer-rates/wholesale-rates/.

[36] M. Mickley and N. Voutchkov. Database of Permitting Practices for Seawater Concentrate Disposal. *Water Intelligence Online*, 15(0):9781780408484–9781780408484, 9 2016. ISSN 1476-1777. doi: 10.2166/9781780408484.

[37] Iris Dimmick. H2Oaks Desalinated Water Passes the Taste Test, 1 2017. URL https://sanantonioreport.org/h2oaks-desalination-plant-latest-in-move-to-diversify-water-sources/#:~:text=The%20cost%20per%20acre%2Dfoot,acre%2Dfoot%20from%20Vista%20Ridge.

[38] David Michel, Amit Pandya, Syed Iqbal Hasnain, Russell Sticklor, and Sreya Panuganti. Water Challenges and Cooperative Response in the Middle East and North Africa. Technical report. URL http://www.

[39] George Joffé. The Impending Water Crisis in the MENA Region. *The International Spectator*, 51(3):55–66, 7 2016. ISSN 0393-2729. doi: 10.1080/03932729.2016.1198069.

[40] Holger Hoff, Christopher Bonzi, Brian Joyce, and Katja Tielbörger. Climate Change, Water and Energy in the MENA Region:
}Why a 'Nexus' Approach is Crucial for Mitigation and Adaptation. *Water (Switzerland)*, 3(3):718–736, 2011. ISSN 20734441. doi: 10.3390/w3030718.

[41] Edoardo Borgomeo, Anders Jägerskog, Amal Talbi, Marcus Wijnen, Mohamad Hejazi, and Fernando Miralles-Wilhelm. Please replace photo with higher-res version. The Water-Energy-Food Nexus in the Middle East and North Africa Scenarios for a Sustainable Future. Technical report. URL www.worldbank.org/water.

[42] L. Bouchaou, J. L. Michelot, A. Vengosh, Y. Hsissou, M. Qurtobi, C. B. Gaye, T. D. Bullen, and G. M. Zuppi. Application of multiple isotopic and geochemical tracers for investigation of recharge, salinization, and residence time of water in the Souss-Massa

aquifer, southwest of Morocco. *Journal of Hydrology*, 352(3-4):267–287, 5 2008. ISSN 00221694. doi: 10.1016/j.jhydrol.2008.01.022.

[43] Dennis Wichelns and Manzoor Qadir. Achieving sustainable irrigation requires effective management of salts, soil salinity, and shallow groundwater. *Agricultural Water Management*, 157:31–38, 7 2015. ISSN 03783774. doi: 10.1016/j.agwat.2014.08.016.

[44] A. Vengosh. Salinization and Saline Environments. In *Treatise on Geochemistry*, pages 325–378. Elsevier, 2014. doi: 10.1016/B978-0-08-095975-7.00909-8.

[45] Mohie El Din Mohamed Omar, Ahmed Moustafa Ahmed Moussa, and Reinhard Hinkelmann. Impacts of climate change on water quantity, water salinity, food security, and socioeconomy in Egypt. *Water Science and Engineering*, 14(1):17–27, 3 2021. ISSN 16742370. doi: 10.1016/j.wse.2020.08.001.

[46] CAPMAS. Final Results of the Population, Housing and Establishments Census 2017. Technical report, Central Agency for Public Mobilization and Statistics (CAPMAS): Arab Republic of, Egypt, 2017.

[47] François Molle, Ibrahim Gaafar, Doaa Ezzat El-Agha, and Edwin Rap. The Nile delta's water and salt balances and implications for management. *Agricultural Water Management*, 197:110–121, 1 2018. ISSN 18732283. doi: 10.1016/j.agwat.2017.11.016.

[48] Metwally Abu-Hamd, Mona Abouhamad, H Abu-Hamd, and Mona M Abouhamad. LIFE CYCLE COST ANALYSIS OF LIGHT STEEL FRAMED BUILDINGS WITH CEMENT-BASED WALLS AND FLOORS. Technical report, 2019. URL `https://www.researchgate.net/publication/339091257`.

[49] Fiona Grant, Carolyn Sheline, Julia Sokol, Susan Amrose, Elizabeth Brownell, Vinay Nangia, and Amos G. Winter. Creating a Solar-Powered Drip Irrigation Optimal Performance model (SDrOP) to lower the cost of drip irrigation systems for smallholder farmers. *Applied Energy*, 323:119563, 10 2022. ISSN 03062619. doi: 10.1016/j.apenergy.2022.119563.

[50] Brian C. McCool, Anditya Rahardianto, Jose I. Faria, and Yoram Cohen. Evaluation of chemically-enhanced seeded precipitation of RO concentrate for high recovery desalting

of high salinity brackish water. *Desalination*, 317:116–126, 5 2013. ISSN 00119164. doi: 10.1016/j.desal.2013.01.010.

[51] Kenneth K.. Tanji and Neeltje C.. Kielen. *Agricultural drainage water management in arid and semi-arid areas*. Food and Agriculture Organization of the United Nations, 2002. ISBN 9251048398.

[52] Paul D. Welle, Josué Medellín-Azuara, Joshua H. Viers, and Meagan S. Mauter. Economic and policy drivers of agricultural water desalination in California's central valley. *Agricultural Water Management*, 194:192–203, 12 2017. ISSN 18732283. doi: 10.1016/j.agwat.2017.07.024.